

May 29, 2015

# Distributions of Ice Supersaturation and Ice Crystals From Airborne Observations in Relation to Upper Tropospheric Dynamical Boundaries

Minghui Diao, *National Center for Atmospheric Research*

Jorgen B. Jensen, *National Center for Atmospheric Research*

Laura L. Pan, *National Center for Atmospheric Research*

Cameron R. Homeyer, *University of Oklahoma*

Shawn Honomichl, *National Center for Atmospheric Research*, et al.

## RESEARCH ARTICLE

10.1002/2015JD023139

## Key Points:

- Ice supersaturation (ISS) and ice crystals occur mostly below thermal tropopause
- High frequencies of ISS and ice crystals occur in vicinity to jet core
- As cirrus evolves, its peak occurrence descends from tropopause to 2–6 km below

## Correspondence to:

M. Diao,  
diao@ucar.edu

## Citation:

Diao, M., J. B. Jensen, L. L. Pan, C. R. Homeyer, S. Honomichl, J. F. Bresch, and A. Bansemer (2015), Distributions of ice supersaturation and ice crystals from airborne observations in relation to upper tropospheric dynamical boundaries, *J. Geophys. Res. Atmos.*, 120, 5101–5121, doi:10.1002/2015JD023139.

Received 23 JAN 2015

Accepted 22 APR 2015

Accepted article online 24 APR 2015

Published online 29 MAY 2015

## Distributions of ice supersaturation and ice crystals from airborne observations in relation to upper tropospheric dynamical boundaries

Minghui Diao<sup>1,2</sup>, Jorgen B. Jensen<sup>2</sup>, Laura L. Pan<sup>3</sup>, Cameron R. Homeyer<sup>4</sup>, Shawn Honomichl<sup>3</sup>, James F. Bresch<sup>5</sup>, and Aaron Bansemer<sup>5</sup>

<sup>1</sup>Advanced Study Program, National Center for Atmospheric Research, Boulder, Colorado, USA, <sup>2</sup>Earth Observing Laboratory, National Center for Atmospheric Research, Boulder, Colorado, USA, <sup>3</sup>Atmospheric Chemistry in the Environment Laboratory, National Center for Atmospheric Research, Boulder, Colorado, USA, <sup>4</sup>School of Meteorology, University of Oklahoma, Norman, Oklahoma, USA, <sup>5</sup>Mesoscale and Microscale Meteorology Laboratory, National Center for Atmospheric Research, Boulder, Colorado, USA

**Abstract** Ice supersaturation (ISS) is the prerequisite condition for cirrus cloud formation. To examine multiscale dynamics' influences on ISS formation, we analyze in situ aircraft observations (~200 m scale) over North America in coordinates relative to dynamical boundaries in the upper troposphere and lower stratosphere. Two case studies demonstrate that ISS formation is likely influenced by mesoscale uplifting, small-scale waves, and turbulence. A collective analysis of 15 flights in April–June 2008 shows that the top layers of ISS and ice crystal distributions are strongly associated with thermal tropopause height. In addition, the average occurrence frequencies of ISS and ice crystals on the anticyclonic side of the jet stream are ~1.5–2 times of those on the cyclonic side. By defining five cirrus evolution phases based on the spatial relationships between ice-supersaturated and in-cloud regions, we find that their peak occurrence frequencies are located at decreasing altitudes with respect to the thermal tropopause: (phase 1) clear-sky ISS around the tropopause, (phase 2) nucleation phase around 2 km below the tropopause, (phases 3 and 4) early and later growth phases around 6 km below the tropopause, and (phase 5) sedimentation/sublimation around 2–6 km below the tropopause. Consistent with this result, chemical tracer correlation analysis shows that the majority (~80%) of the earlier cirrus phases (clear-sky ISS and nucleation) occurs inside the chemical tropopause transition layer, while the later phases happen mostly below that layer. These results shed light on the role of dynamical environment in facilitating cirrus cloud formation and evolution.

### 1. Introduction

Cirrus clouds are the type of clouds that are composed of ice crystals, and they are usually in the form of filaments, patches, or narrow bands, according to the cloud classification of World Meteorological Organization [WMO, 1975, 1987]. Although the total water content of cirrus clouds is often 1–2 orders of magnitude smaller than that of low-level clouds (such as stratus clouds) [Liou, 1992], cirrus clouds are located at altitudes where the atmospheric radiative forcing is most sensitive to perturbations in water vapor concentration. For example, Solomon *et al.* [2010] showed that a perturbation of 1 ppmv water vapor in a 1 km layer around the tropopause can lead to an instantaneous effect of  $\sim +0.10 \text{ W m}^{-2}$  on surface climate through longwave radiation. Such increase of longwave radiative forcing is 5 times of that caused by a 1 ppmv water vapor perturbation at 2 km below the tropopause ( $\sim 0.02 \text{ W m}^{-2}$ ). In addition to water vapor, the solid phase of water (e.g., ice crystals in cirrus clouds) in the upper troposphere and lower stratosphere (UT/LS) also plays an important role in modulating the Earth's climate system. Cirrus clouds influence the partitioning between vapor and ice, as well as the dehydration of air in the UT/LS region [Jensen *et al.*, 2013a; Randel and Jensen, 2013]. In addition, the formation of cirrus clouds is under the influence of anthropogenic activities, such as aerosol emissions [Cziczo *et al.*, 2013] and global climate perturbations [Kärcher and Spichtinger, 2009]. Thus, characterizing the formation and evolution of cirrus clouds is important for providing an accurate estimation of water vapor and ice crystal concentrations in the UT/LS.

Due to the highly variable nature of cirrus clouds in space and time, it is currently challenging to represent their spatial heterogeneities on the grid-box scale in climate models. In the development of more realistic simulations/parameterizations of cirrus clouds, an important step is to understand the controlling

processes and conditions of their formation and evolution. In particular, much effort has been undertaken to improve model representations of the birthplaces of cirrus clouds—regions of ice supersaturation (ISS, where relative humidity with respect to ice, RH<sub>i</sub>, is greater than 100%) [Kärcher and Burkhardt, 2008; Gettelman et al., 2012]. The ISS conditions, combined with dynamical processes and aerosol distributions, largely determine the subsequent formation of cirrus clouds and their microphysical properties. In addition, although ISS is the prerequisite condition for ice crystal formation, the two scenarios (clear-sky ISS versus cirrus clouds) have very different radiation effects. For example, differences of up to  $\sim 3 \text{ K d}^{-1}$  in the vertical net heating rate and up to  $\sim 41 \text{ W m}^{-2}$  in the net surface radiative budget are found when comparing the two scenarios [Fusina et al., 2007]. Thus the controlling mechanisms for the transition from ISS to ice crystals are relevant information for both cloud microphysical processes and radiation effects.

The formation and evolution from clear-sky ISS to cirrus clouds involves multiscale dynamical processes, which not only influence their macroscopic structure such as horizontal and vertical extent but also influence their microphysical properties. On the microscale, in situ aircraft observations ( $\sim 200 \text{ m}$  horizontal scale) have demonstrated that the characteristics of ice-supersaturated regions (ISSRs, where ISS is spatially continuously observed), such as location and RH<sub>i</sub> magnitude, are dominated by water vapor horizontal variability as opposed to temperature variability [Diao et al., 2014a]. In addition, cloud model studies have shown that the formation of ISS and ice crystals is influenced by small-scale dynamics, such as vertical velocity perturbations [Spichtinger and Gierens, 2009a], eddies and turbulence [Fusina and Spichtinger, 2010], and gravity waves [Spichtinger and Krämer, 2013]. At larger scales, model simulations have shown that mesoscale to synoptic scale dynamics, such as mesoscale gravity waves [Spichtinger et al., 2005b] and warm conveyor belts [Spichtinger et al., 2005a], can provide large-scale uplifting and cooling, leading to ISSR formation. However, most of the previous analyses of ISSRs are either based on in situ observations without simultaneous analysis of dynamics on the larger scales [Diao et al., 2014a, 2014b] or based on modeling data [Spichtinger et al., 2005a, 2005b] that did not provide high-resolution information on ISS and ice crystal properties. The goal of this work is to link the microscale observations with the multiscale scale dynamical background to examine cirrus cloud formation in association with multiscale processes.

The tropopause and jet stream are two fundamental dynamical features in the UT/LS region. The tropopause is a distinct thermodynamic boundary that separates the relatively stable stratosphere from the more convectively mixed troposphere. The jet streams mark the boundary between the stratosphere and troposphere along the isentropic surface and are often associated with sharp decreases in the tropopause height [e.g., Palmén and Newton, 1969; Shapiro and Gronas, 1999]. Furthermore, Tilmes et al. [2010] showed that using the subtropical jet core and polar jet core defined by the local maximum of zonal wind speed, the distributions of tropopause height (given in potential temperature) can be separated into three regimes: the tropics, subtropics, and the polar regions. In addition to the relationship between tropopause height variations and jet stream locations, previous studies have shown that the locations of tropopause and jet streams are often associated with strong gradient in the distributions of chemical tracers in the UT/LS, such as ozone [Hudson et al., 2003; Ray et al., 2004; Brioude et al., 2008] and water vapor [Follette-Cook et al., 2009; Zahn et al., 2014].

Due to the strong correlation between the spatial characteristics of ISSRs and the water vapor field [Diao et al., 2014a], a main goal of this work is to relate the distributions of ISS and ice crystals to the locations of tropopause and jet cores, since sharp variations in water vapor field have been frequently observed around those regions [e.g., Follette-Cook et al., 2009; Zahn et al., 2014]. In addition, the clear-air turbulence near the jet core [e.g., Shapiro, 1976; Jaeger and Sprenger, 2007] combined with the strong temperature gradient across the tropopause can provide the potential dynamical and thermal background for ISS and ice crystal formation. Further, due to their radiative effects, cirrus clouds can also interact with the thermal and dynamical background, such as modifying the structure of tropopause region [Hartmann et al., 2001; Yang et al., 2010]. Given the unique roles of tropopause and jet streams in the UT/LS and their interactions with cirrus clouds, a quantitative analysis of cirrus clouds' formation and evolution relative to these two dynamical boundaries would provide valuable information for cirrus cloud simulations.

Previous investigations on the spatial distributions of cirrus clouds in the UT/LS region are mostly based on satellite remote sensing observations [Kahn et al., 2008, 2014; Massie et al., 2010; Riihimäki and McFarlane,

2010; Pan and Munchak, 2011]. For example, based on a 4 year data set from the Cloud-Aerosol Lidar and Infrared Pathfinder Satellite Observations, Pan and Munchak [2011] showed that the cloud top height of cirrus clouds is highly correlated with the location of thermal tropopause. In addition, based on the NASA CloudSat data, cirrus clouds aloft in the UT have been observed on the leading edge of frontal systems associated with extratropical cyclones [Posselt et al., 2008]. As the prerequisite condition for cirrus cloud formation, ISS distribution has also been analyzed based on remote sensing observations. For example, previous studies based on the NASA Atmospheric Infrared sounder (AIRS) observations showed that the highest occurrence frequency of ISS over Northern Hemisphere midlatitudes happens near pressures of 250–300 mb [Lamquin et al., 2012] and altitudes of 10–12 km [Kahn et al., 2009]. In addition, based on the NASA AIRS data, Gettelman et al. [2006] qualitatively reported that the high values of RHi are often found on the edge of the frontal cloud bands. According to the global observations of Microwave Limb Sounder, Spichtinger et al. [2003] compared the occurrence frequencies of ISSRs between two pressure levels (i.e., 215 hPa and 147 hPa) and found that ISSRs occur more frequently at 215 hPa than 147 hPa around the midlatitude storm tracks. Although the authors did not directly relate such variation in the occurrence frequencies of ISSRs to the location of tropopause, their finding suggests an influence of tropopause height on the ISSR distributions. In addition to the satellite observations, a modeling study by Gierens and Brinkop [2012] analyzed the distribution of relative vorticity inside ISSRs based on the forecast data from the European Centre for Medium-Range Weather Forecasts (ECMWF) over 4 months. The authors showed that the ISSRs over Europe are associated more often with anticyclonic systems than cyclonic systems, while no statistically significant skewness was found for the relative vorticity distribution inside tropical ISSRs. Due to the limitations in spatial resolution of satellite observations and model simulations, additional in situ observations are required for analyzing distributions of small-scale ISSRs.

In this work, 1 s resolution, in situ observations of ISS and ice crystals from an aircraft-based flight campaign are analyzed in connection to the meteorological field in the UT/LS. In order to provide a collective analysis of the relatively scattered aircraft observations, we introduce an approach to group the in situ observations into a set of dynamical coordinates based on their spatial relationship with two dynamical boundaries—the thermal tropopause and jet core. The location of tropopause and jet core is derived from the National Centers for Environmental Prediction (NCEP) Global Forecast System (GFS) model analyses. Furthermore, using chemical tracer relationships derived from in situ measurements, we identify air masses in relation to the transition layer around the chemical tropopause, where the mixing of stratosphere and troposphere dominates. The chemical tracer analysis therefore provides a diagnosis of air mass mixing on the development of ISS and ice crystals. The analyses using dynamical coordinates and tracer-tracer correlation complement each other in providing information on the background conditions of ISS and ice crystal formation and evolution.

## 2. Data Set and Instrumentations

### 2.1. Stratospheric-Tropospheric Analyses of Regional Transport 2008 Campaign and Instrumentation

In this study we use 1 Hz (~230 m) aircraft-based observations from the National Science Foundation (NSF) Gulfstream-V (GV) research aircraft during the NSF Stratospheric-Tropospheric Analyses of Regional Transport 2008 (START08) campaign [Pan et al., 2010]. The START08 campaign includes 18 flights during the period of 18 April to 27 June 2008. The GV aircraft primarily targeted the extratropical UT/LS region over North America (25°N–63°N, 86°W–118°W), with flights almost exclusively over land. For this work, we analyze the observations from research flights (RF) 04–18, for which high-quality water vapor measurements are available. The combined data set of RF04–18 provides about 100 h of observations, including ~90 transects across the extratropical thermal tropopause. All analyses of ISS and ice crystals are restricted to temperatures  $\leq -40^{\circ}\text{C}$  in order to exclude the mixed phase clouds (i.e., those with both supercooled liquid droplets and ice crystals).

Table 1 summarizes the accuracy and precision of the instrumentation that have been used in this work. Water vapor measurements are obtained by the 25 Hz, open-path vertical cavity surface-emitting laser (VCSEL) hygrometer [Zondlo et al., 2010]. The water vapor measurements are averaged to 1 s for consistency with the in situ temperature measurements. The accuracy and precision of water vapor measurements are 6% and  $\leq 1\%$ , respectively. Temperature was recorded by a Rosemount total temperature probe (deiced model 102 LA) with accuracy and precision of  $\sim \pm 0.5\text{--}1\text{ K}$  and 0.01 K,

**Table 1.** Summary of Instrumentation Accuracy and Precision During the START08 Campaign

Instrument	Measurement	Accuracy	Precision	
VCSEL hygrometer	H <sub>2</sub> O mixing ratio	6%	≤1%	
Rosemount total temperature probe (deiced model 102 LA)	Temperature	~±0.5–1 K	0.01 K	
Chemiluminescent reaction detector	O <sub>3</sub>	±(2 ppbv + 5%)	0.1 ppbv	
NCAR vacuum ultraviolet resonance fluorescence instrument	CO	9%	0.8 ppbv	
Honeywell LASEREF IV Inertial Reference Unit, radome pressure, static pressure, pitot tubes, temperature probe, and differential Global Positioning System	Vertical wind velocity	~±0.15–0.30 m/s	~0.01 m/s	
Ice particle measurement	Measurement range	Utilized range for in-cloud detection	Utilized range for analysis of ice crystal number concentration and mean diameter	Concentrations of a single particle count at typical GV air speed (~200 m/s)
SID_2H	5–50 μm	10–50 μm	10–50 μm	15 L <sup>-1</sup>
Fast-2DC	25–1600 μm	50–1600 μm	100–1600 μm	0.1 L <sup>-1</sup> at 100 μm and 0.03 L <sup>-1</sup> at 1 mm

respectively. For the sampling range of 233 K–196 K in the START08 campaign, the combined uncertainties from the temperature and water vapor measurements lead to uncertainties in RHi of ~8–18%. Most (~95%) of the ISS observation happen at temperature above -59°C, which have ~8–16% uncertainties in ISS. The probability density function (PDF) of the in-cloud RHi observations peaks around 100% [Diao *et al.*, 2014a], which is consistent with previous 1 Hz aircraft observations [Ovarlez *et al.*, 2002; Krämer *et al.*, 2009]. We conducted sensitivity tests on our analysis for temperature ±0.5 K and RHi ± 15%. Although details of the vertical occurrence frequency distributions of ISS are quite sensitive to such variation, our basic conclusions on the relationships between the ISS distribution and the thermal tropopause height do not vary.

Ozone measurements are obtained from the chemiluminescent reaction detector, which has a detection limit below 0.1 ppbv and an uncertainty estimated at ±(2 ppbv + 5%) for 1 Hz data [Ridley *et al.*, 1992]. Carbon monoxide (CO) measurements are obtained from the National Center for Atmospheric Research (NCAR) vacuum ultraviolet resonance fluorescence instrument with an accuracy of 9% and precision of 0.8 ppbv [Gerbig *et al.*, 1999]. The vertical wind speed is measured by a combination of measurements (as shown in Table 1) with an accuracy of ~±0.15–0.30 m/s and a resolution of ~0.01 m/s.

Ice crystals measurements used in this study come from two probes: the Small Ice Detector Probe (SID-2H) instrument [Cotton *et al.*, 2010] with a measurement range of 5–50 μm and the modernized Fast 2-Dimensional Cloud particle imaging (Fast-2DC) probe with a 64-diode laser array and 25 μm resolution for a measurement range of 25–1600 μm. A quality control procedure is applied to SID-2H data to minimize particles generated by noise or aerosols [Johnson *et al.*, 2014], by filtering out particles with low light scattering intensity, thus effectively limiting the sensitivity of the SID-2H to particles with diameter of approximately 10 μm or larger. The combined measurements of SID-2H and 2DC are used for the discrimination between measurements with and without ice crystals, which are also labeled as the “in-cloud” and “clear-sky” conditions for 1 Hz aircraft observations, respectively. When either of the two ice probes has detected at least one ice crystal within 1 s, we define this second as in-cloud condition. Typically, the in-cloud conditions detected by 2DC and SID-2H have concentrations of ice crystals at 0.03–2000 L<sup>-1</sup> and 15–1 × 10<sup>4</sup> L<sup>-1</sup>, respectively. The concentration of a single particle count at a typical GV air speed (~200 m/s) is about 15 L<sup>-1</sup> for SID\_2H. The Fast-2DC has a size-dependent sample volume, so a single count represents a concentration ranging from 0.1 L<sup>-1</sup> at 100 μm to 0.03 L<sup>-1</sup> at 1 mm. Based on instrument simulations, the estimated uncertainty of measured ice crystal number concentration is up to a factor of ~2.0. Ice water content (IWC) in two case studies of RF04 and RF11 are derived from 2DC data based on the mass-dimensional relationship given in Brown and Francis [1995]. For analyses of ice crystal number concentration (Nc) and volume-weighted mean diameter (Dc), we exclude ice crystals smaller than 100 μm in 2DC measurements to minimize shattering effects and optical uncertainties in 2DC Nc and Dc data. We note that the distinction between clear-sky and in-cloud is not influenced by the overlapping size range of SID-2H and 2DC or shattering effects, since the only requirement for this classification is the presence of an ice crystal.

In this work, ice-supersaturated regions (ISSRs) are defined as regions where ISS is observed to be spatially continuous, including both clear-sky and in-cloud conditions. This definition is consistent with the previous definition of ISSRs [Spichtinger *et al.*, 2005b]. Ice crystal regions (ICRs) are defined as the regions where ice

crystals are spatially continuously observed based on the in-cloud definition, consistent with the previous definition by *Diao et al.* [2013]. Here ICRs represent quasi-horizontal, 1-D segments of cirrus clouds, since the aircraft true air speed is always at least 20 times higher in the horizontal direction than the vertical direction. The final data set has ~60.5 flight hours at  $T \leq -40^\circ\text{C}$ , including ~2.3 h of ISS and ~3.1 h of ICR observations. The overlap between ISSRs and ICRs is ~1.3 h.

## 2.2. NCEP GFS Analyses

The NCEP Global Data Assimilation System analyses for the GFS spectral model (hereafter simply, GFS) were used to provide meteorological context for this study. The GFS analyses were obtained in real time from NCEP and archived at NCAR. The analyses have a horizontal resolution of  $0.3125^\circ$  with 47 pressure levels in the vertical, providing a resolution of about 500 to 1000 m in the UT/LS region. The GFS analyses are available every 6 h, beginning at 00:00 UTC.

## 3. Method

### 3.1. Jet Core Identification and Horizontal Jet Core Coordinate

While the tropopause separates the UT from LS air mass vertically, the jet streams and associated frontal zone often create air mass discontinuity in horizontal. A number of different studies used jet core relative coordinates. *Ray et al.* [2004] used relative wind speed in the vicinity of jet maximum as a coordinate to analyze ozone distribution across the jet. *Tilmes et al.* [2010] used jet streams to separate air mass regimes and derive a trace gas climatology based on aircraft data. *Manney et al.* [2011] derived a jet core climatology and showed that the tropopause and jet relative coordinates can provide a dynamically consistent average of chemical tracer field. Taking a similar approach as *Manney et al.* [2011], we use the maximum horizontal wind speed ( $U_{\text{max}}$ ) from GFS data to identify the jet core locations. The identification includes three steps: first, the locations where horizontal wind speed  $\geq 30$  m/s are found; second, among these locations,  $U_{\text{max}}$  locations are identified as where the bin values of horizontal wind speed (binned by 5 m/s) are higher than those in their adjacent regions. In each longitudinal or latitudinal vertical cross sections, there might be multiple  $U_{\text{max}}$  identifications, since the subtropical and polar jet streams may coexist over the sampling domain during the late spring/early summer period. In fact, during this period, the polar and subtropical jets usually have a meandering shape, and though usually separate, they merge into one jet stream in some locations [e.g., *Tilmes et al.*, 2010]. Finally, we filter out  $U_{\text{max}}$  of negligibly small horizontal scale ( $\leq \sim 1^\circ$  in latitude and longitude), and the remaining  $U_{\text{max}}$  is defined as jet core. More than one jet core will be defined if the two  $U_{\text{max}}$  locations are at least  $\sim 1^\circ$  apart in latitude and longitude; otherwise, only the highest  $U_{\text{max}}$  is used to define the jet core. A slight difference from the approach by *Manney et al.* [2011] is that we search for  $U_{\text{max}}$  not only in meridional transect but also in zonal transect. This modification allows the consideration of the meandering shape of the jet, which has both zonal and meridional components.

After identifying the jet core, we calculate the horizontal arc distance between 1 Hz aircraft observations and the closest jet core locations. The distribution of arc distances (in degree) of all aircraft observations ( $T \leq -40^\circ\text{C}$ ) with respect to the jet core is shown by the abscissa in Figures 1a and 1b, where positive distances refer to observations on the cyclonic side of the jet and negative distances refer to the anticyclonic side.

### 3.2. Vertical Thermal Tropopause Relative Coordinate

In the analyses of the vertical distribution of in situ observations, we use a modified thermal tropopause relative altitude as the vertical coordinate following the definition given in *Pan and Munchak* [2011]. Specifically,  $Z_r$  is calculated as

$$Z_r = \bar{Z}_{\text{trop}} + (Z - Z_{\text{trop}}), \quad (1)$$

where  $Z$  is the aircraft altitude with respect to sea level,  $Z_{\text{trop}}$  is the tropopause height collocated with the aircraft observation, and  $\bar{Z}_{\text{trop}}$  is the average thermal tropopause height for all 15 flights. The distribution of  $(Z - Z_{\text{trop}})$  is shown by the ordinate in Figure 1a, where positive values refer to aircraft measurements above the tropopause. In comparison, the ordinate in Figure 1b shows the relative altitudes ( $Z_r$ ) of 1 Hz in situ observations in tropopause relative coordinate, i.e., adding  $\bar{Z}_{\text{trop}}$  to  $(Z - Z_{\text{trop}})$  as shown by equation (1). The tropopause relative coordinate is useful for averaging vertical profiles with various tropopause heights, as

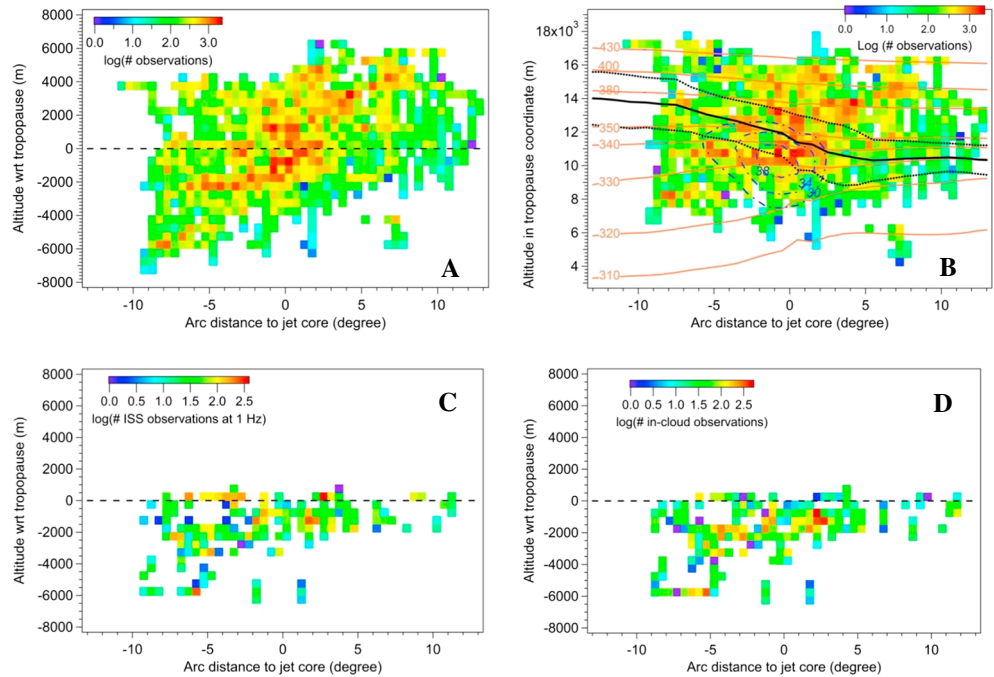


**Figure 1.** Number of 1 Hz observations for START08 research flight (RF) 04–18 at  $T \leq -40^\circ\text{C}$ . (a) Distribution of in situ observations with respect to the thermal tropopause and jet core. The negative (positive) altitudes show observations below (above) the tropopause, and the negative (positive) arc distances show observations on the anticyclonic (cyclonic) side of the jet core. (b) The abscissa is the same as Figure 1a, but the ordinate is replaced by the tropopause relative coordinate (i.e., shifting the flight altitudes with respect to the collocated tropopause by adding the average tropopause height). The average profiles of tropopause height (in meter, black line), potential temperature (in K, orange contours), and horizontal wind speed (in m/s, dot-dashed blue contours) are derived from the vertical profiles during the 15 flights. The  $\pm 1$  standard deviation of tropopause height is shown in dotted lines. For both Figures 1a and 1b, the total number of observations is shown in log scale for each  $500\text{ m} \times 0.5^\circ$  bin. (c and d) The number of 1 Hz ISS and in-cloud samples in altitudes relative to tropopause, respectively.

previously demonstrated by Birner *et al.* [2002]. We note that due to such shift, the values of  $Z_r$  are generally not the same as the real aircraft altitude ( $Z$ ).

The average atmospheric conditions (including  $\bar{Z}_{\text{trop}}$ , potential temperature, and horizontal wind speed) are derived from the vertical cross sections through each 1 s aircraft observation and its closest jet core. The atmospheric conditions of these vertical cross sections are extracted from the GFS data, and their horizontal scales are referenced to the jet core coordinate. Since each flight has different sample sizes, we first calculate the mean vertical profiles for individual flights and then average them over 15 flights to avoid overrepresenting a certain flight.  $\bar{Z}_{\text{trop}}$  is shown in Figure 1b (thick black line), with the  $\pm 1$  standard deviation for the 15 flights shown in black dotted lines. In addition, the average horizontal wind speed (dot-dashed blue line) around the jet core has the maximum value around 38 m/s. The  $\sim 330\text{ K}$  isentropic contour (orange line) intersects the jet core center, suggesting that this jet core coordinate has a main feature of the polar jet, and there is also partial merging with the subtropical jet [Keyser and Shapiro, 1986; Tilmes *et al.*, 2010].

**Table 2.** Definition of Five Evolution Phases of In Situ Samples of Cirrus Clouds (Based on Diao *et al.* [2013])

Five Evolution Phases	Definition
Clear-sky ice-supersaturated regions (ISSRs)	Spatially continuous ISSRs in clear-sky condition
Nucleation phase	Partially in-cloud segments buried inside the ISSRs
Early growth phase	ISSRs and in-cloud regions intersecting each other
Later growth phase	Partially ice-supersaturated segments buried inside the in-cloud regions
Sedimentation/sublimation	In-cloud regions at subsaturation and/or saturation conditions

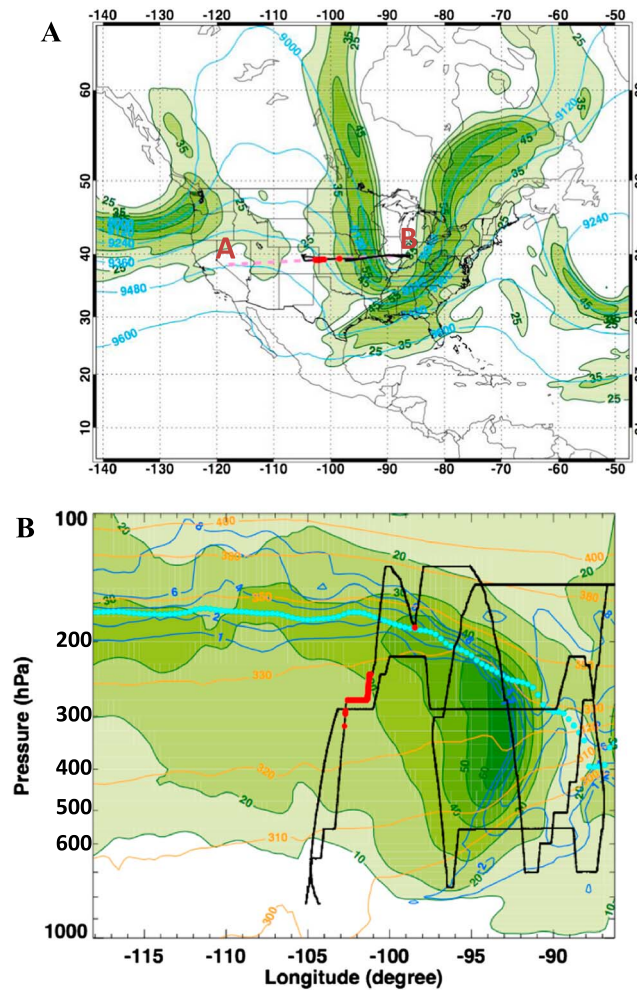


**Figure 2.** (a) The 18:00 UTC GFS 300 hPa analysis for RF04. Horizontal wind speed (25–55 m/s binned by 5 m/s, green shaded) and geopotential height (m, light blue). The light pink dashed line in Figure 2a shows the A–B transect that is plotted in Figure 2b. (b) GFS vertical cross section along line A–B of horizontal wind speed (10–60 m/s binned by 10 m/s, green shaded). The light blue dots show the thermal tropopause. The dark blue lines show contours of potential vorticity unit (PVU). The orange lines show the potential temperature (K). In both Figures 2a and 2b, the thick black line shows the flight track. At the time of ISS observations (red dots), the flight was heading eastward.

We note that the aircraft generally maintains the same pressure altitudes when flying horizontal legs, which results in more sampling above the tropopause on the cyclonic side than the anticyclonic side due to the tropopause height change between the two sides. The total number of ISS and ice crystal samples is shown in altitude with respect to tropopause in Figures 1c and 1d, respectively.

### 3.3. Phases of ISSR and ICR Evolution

Based on the method from *Diao et al.* [2013], we separate five phases of cirrus cloud development from 1-D Eulerian observations into a quasi-evolutionary view. An ISSR+ICR sample is used to represent a horizontal transect of cirrus clouds, which is defined as the region with spatially continuous observations of either ISS or ice crystals. The five phases of ISSR+ICR evolution include (1) clear-sky ISSRs, (2) ice crystal nucleation, (3) early growth, (4) later growth, and (5) sedimentation/sublimation. As shown in Table 2, the nucleation phase is defined as where ICRs reside inside the ISSRs, while the early growth phase is where ICRs and ISSRs intersect each other, and the later growth phase is where ISSRs reside inside ICRs. Finally the sedimentation/sublimation phase has all RH<sub>i</sub> values relaxed to saturation and/or subsaturation inside ICRs. This method helps to provide an evolutionary view of cirrus clouds based on the in situ observed spatial characteristics of ISSRs and ICRs. Totally, there are 779 cases of ISSR+ICR samples, and the number of Phases 1–5 is 104, 31, 48, 35, and 561, respectively.

## 4. Case Studies: Dynamical Background of ISS Formation

### 4.1. Meteorological Conditions Observed in RF04 and RF11

To demonstrate the ISS and cirrus cloud formation under different dynamical conditions, we identified two cases from START08 flights, RF04 and RF11, which represent two dynamical regimes associated with ISS formation: (1) mesoscale uplifting and (2) small-scale waves and turbulence, respectively. RF04 took place on 28 April 2008, and a stratospheric intrusion occurred over southern Illinois and Indiana around the time of the flight. The synoptic scale dynamical setting for RF04 is given in Figure 2. The 18:00 UTC 300 hPa GFS analysis (Figure 2a) shows a highly amplified ridge-trough pattern with the polar jet crossing the upper midwest on the back side of the trough centered at 89°W and extending into the Gulf Coast states, where it partially merged with the subtropical jet and then extended northward into eastern Canada. The upstream ridge centered along 115°W was characterized by relatively lighter winds. The ISS observations occurred around 21:20 UTC (around 39°N, 102°W) on the anticyclonic side of the polar jet between the trough and the upstream ridge.

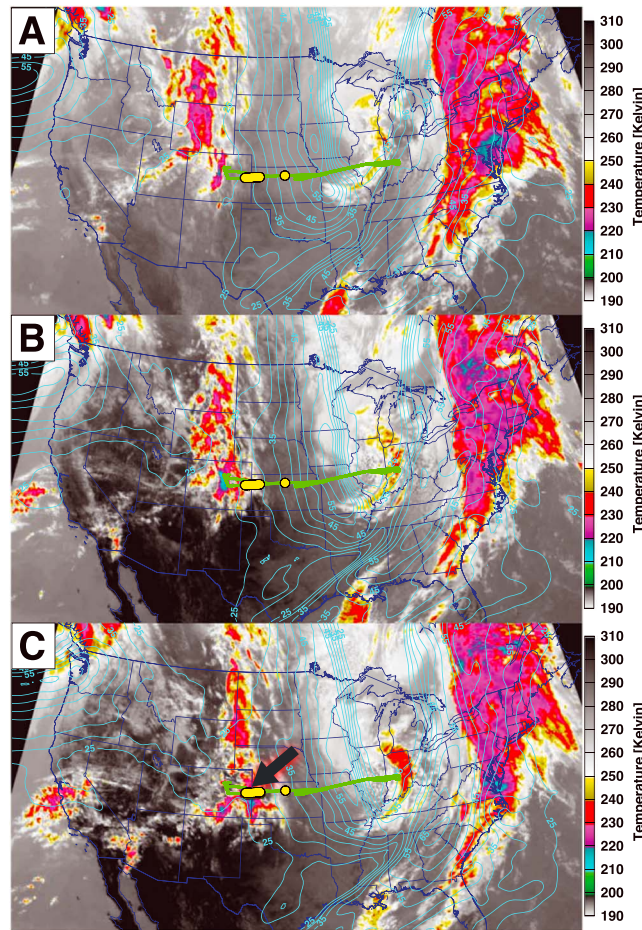


**Figure 3.** GOES 12 thermal-IR satellite images over the U.S. The UTC time stamps are (a) 15:00, (b) 18:00, and (c) 21:00 UTC. The GV track is shown in thick green line, and the ISS observations are shown in yellow dots. The azure contours show the 300 hPa horizontal wind speed. The color bar shows the decreasing cloud top temperatures from  $-10^{\circ}\text{C}$  (grey),  $-40^{\circ}\text{C}$  (red/pink), to  $-60^{\circ}\text{C}$  (blue/green). The black arrow illustrates ISS observations that happened almost at the same time as the GOES 12 imagery of that panel.

ISS occurrences are closely related to the tropopause location and are in the region of strong PV gradient (Figure 4b), indicating a stronger influence from the stratospheric air mass than those observed in RF04.

GOES 12 infrared satellite imagery (Figure 5) shows that the cirrus cloud top temperatures warmed over the Idaho/Montana/Wyoming region during the morning. Along the flight track, where the ISS segments were observed around 18:30–18:50 UTC (Figure 5c, marked by black arrow), cloud top temperatures increased from  $\sim -35^{\circ}\text{C}$  to  $\sim -20^{\circ}\text{C}$  (color changes from yellow to grey/white). The increase in cloud top temperature implies that no obvious large-scale uplifting was present in the GOES 12 imagery, but we caution that the vertical wind field can change rapidly, which might not be fully captured by the discontinuous GOES 12 imagery.

**4.2. Air Mass Identification of ISS Observations in RF04 and RF11 Based on Chemical Tracer-Tracer Correlations**

The difference in the dynamical regimes where ISS was observed in RF04 and RF11 can be identified in the tracer-tracer space using simultaneously sampled chemical tracers of ozone ( $\text{O}_3$ ), water vapor ( $\text{H}_2\text{O}$ ),

The vertical dimension of the flight and the dynamical field is given in Figure 2b (along the A–B transect in Figure 1a). The jet core is located around  $93^{\circ}\text{W}$  with a horizontal wind speed maximum of  $\sim 60\text{ m/s}$ . Animations of GOES 12 thermal-IR imagery for 27 and 28 April 2008 showed extensive cirrus within the ridge as it entered the West Coast of the United States. Brightness temperatures of the cirrus increased as the cirrus moved into the intermountain west but cooled as the clouds crossed central Colorado ( $\sim 39^{\circ}\text{N}$ ,  $105^{\circ}\text{W}$ ) prior to 15:00 UTC indicating orographic enhancement, that is, uplifting. Images from 15:00, 18:00, and 21:00 UTC are shown in Figure 3. The coldest cloud tops, suggesting enhanced mesoscale upward motion, coincided with the GV flight track and ISS observations near the Colorado-Kansas border at 21:20 UTC.

RF11 took place on 14 May 2008 and similar to RF04, a stratospheric intrusion descended below the polar jet stream around the time of the flight. The jet developed over the west coast of Canada and the northwest U.S. in the north-south direction. The 18:00 UTC 300 hPa GFS analysis (Figure 4a) illustrates that the GV intersected the jet in the east-west direction over Montana. In contrast to RF04, ISS observations in RF11 were mostly found in the vicinity of the jet. The vertical cross section of the flight shows that the

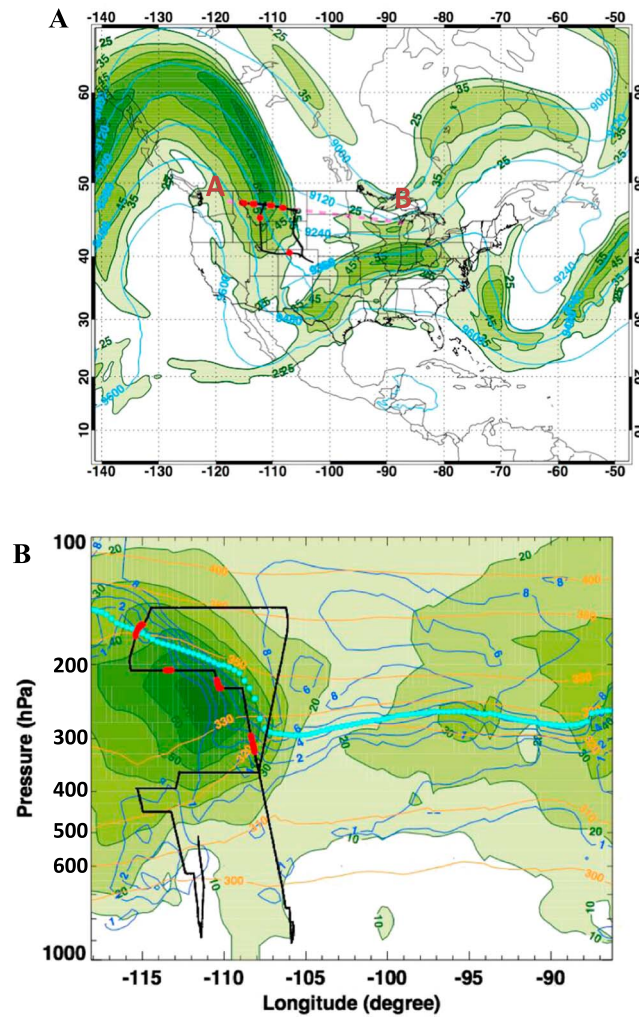


**Figure 4.** Similar to Figure 2 but for RF11. Around the time of ISS observations (red dots), the flight was heading westward.

and carbon monoxide (CO). The relationship of these tracers,  $O_3$ -CO (Figures 6a and 6b) and  $O_3$ -H<sub>2</sub>O (Figures 6c and 6d), provides unique information that complements the large-scale meteorological information since the chemical tracers are sampled at the same scale as the microphysical variables. CO and H<sub>2</sub>O are generally used as the tropospheric tracers, since the troposphere is the significant source region for the two species. For the same reason,  $O_3$  is considered as a stratospheric tracer. The relationship of stratospheric versus tropospheric tracers has been demonstrated to form an “L”-shaped distribution in the UT/LS region [e.g., Fischer et al., 2000; Pan et al., 2004, 2007; Konopka and Pan, 2012]. As described in these previous works referenced, the tracer-tracer relationship identifies three types of behaviors, and they are referred to as the “stratospheric branch” (low CO/H<sub>2</sub>O and large variability of  $O_3$ ), “tropospheric branch” (low  $O_3$  and large variability of CO/H<sub>2</sub>O), and the mixed or transitional air mass between the two branches (the mixing layer or the extratropical tropopause transition layer). Thus, using the relationships between  $O_3$ , CO, and H<sub>2</sub>O, we can discern the tropospheric and stratospheric reservoirs and lines of

mixing between the two. Notably, the tropospheric reservoir is often characterized by  $O_3 < 100$  ppbv and widely varying CO and H<sub>2</sub>O, while the stratospheric reservoir is often characterized by widely varying  $O_3$  at  $CO < 50$  ppbv and  $H_2O < 10$  ppmv [e.g., Fischer et al., 2000; Pan et al., 2004].

The tracer-tracer relationships for ice-supersaturated and in-cloud segments are compared between RF04 (Figures 6a and 6c) and RF11 (Figures 6b and 6d), which represent associations with tropospheric-tropospheric mixing and stratospheric-tropospheric mixing, respectively. In RF04, both  $O_3$ -CO and  $O_3$ -H<sub>2</sub>O relationships show that ISS was observed almost exclusively in the troposphere. The relatively straight, positively correlated  $O_3$ -CO and  $O_3$ -H<sub>2</sub>O relationships (Figures 6a and 6c) indicate that a two-level mixing had happened at the regions with ISS (Appendix B of Diao et al. [2014a]). That is, the air masses originated from lower levels in the troposphere with high  $O_3$  and CO (H<sub>2</sub>O) and were uplifted to higher levels in the troposphere, subsequently mixing into air masses with low  $O_3$  and CO (H<sub>2</sub>O) concentrations.

In RF11, ISS follows mixing lines with negative slopes extending from the tropospheric reservoir toward the stratospheric reservoir, which indicates mixing between the stratosphere and troposphere. Such influences from stratospheric air masses are in agreement with the finding that ISS observations in RF11 were located along the dynamical boundary of the stratospheric intrusion (as shown in Figure 4b). Taken together, these two cases show that ISS generated by mesoscale uplifting versus small-scale waves and turbulence both involve substantial mixing between air masses, including stratosphere-

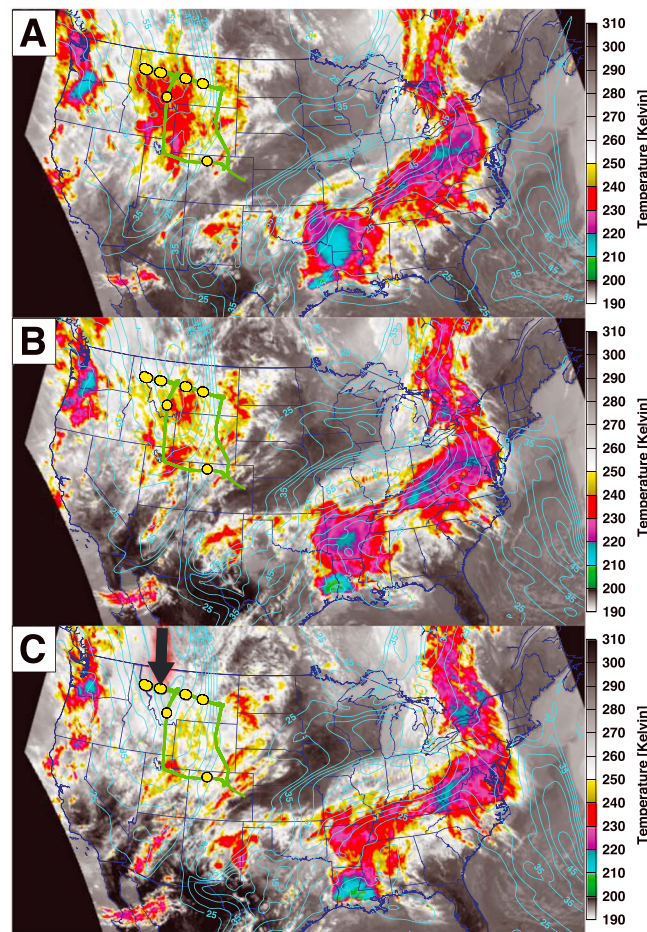


**Figure 5.** Similar to Figure 3 but for RF11. The UTC time stamps are (a) 15:45, (b) 17:15, and (c) 19:02 UTC. The color bar shows the increasing cloud top temperatures from  $-35^{\circ}\text{C}$  (yellow),  $-20^{\circ}\text{C}$  (white), to  $-10^{\circ}\text{C}$  (grey).

which is about 1 order of magnitude smaller than the updraft speed in RF04. In addition, RF11 shows apparent gravity wave structure with a wavelength of  $\sim 30$  km (18:36:40–18:45:00 UTC) and small-scale turbulence (e.g., 18:45:00–18:47:30 UTC and 18:49:10–18:51:40 UTC) around the stratospheric intrusion. In fact, according to previous work [Shapiro, 1976], the locations of ISS in RF11 coincide with regions of expected clear-air turbulence, i.e., the region around the jet core on the cyclonic side. The mesoscale uplifting scheme in RF04 is consistent with the previous case study of a large-scale uplifting condition in a warm conveyor belt [Spichtinger et al., 2005a], while the results from RF11 showed that other conditions involving small-scale vertical velocity perturbations due to waves and/or turbulence can also generate ISS. These results point out the importance of understanding dynamical conditions below the mesoscale.

The ice microphysical properties of two flights are compared in terms of IWC,  $N_c$ , and  $D_c$ . The IWC observed in RF04 (Figure 7b) is significantly ( $\sim 1$ – $2$  orders of magnitudes) higher than those observed in RF11 (Figure 8b). In addition, the  $N_c$  and  $D_c$  values observed in RF04 typically are  $\sim 10^5$ – $10^6$   $\text{m}^{-3}$  and  $30$   $\mu\text{m}$  (SID-2H),  $\sim 10^4$ – $10^5$   $\text{m}^{-3}$  and  $125$ – $1500$   $\mu\text{m}$  (2DC), respectively (Figure 7c). In comparison, the  $N_c$  and  $D_c$  observed in RF11 are  $\sim 10^4$ – $10^5$   $\text{m}^{-3}$  and  $20$ – $40$   $\mu\text{m}$  (SID-2H),  $\sim 10^2$ – $10^3$   $\text{m}^{-3}$  and  $125$ – $660$   $\mu\text{m}$  (2DC), respectively (Figure 8c). These results show that the  $N_c$  values observed in RF04 are about  $\sim 1$ – $2$  orders of magnitudes higher than those observed in RF11 for both  $1$ – $50$   $\mu\text{m}$  and  $100$ – $1600$   $\mu\text{m}$  measurements ranges, while the  $D_c$  values between RF04 and RF11 are similar. The higher IWC and  $N_c$  values in RF04 are consistent with the fact that RF04 is characterized by broader and stronger uplift.

troposphere mixing and troposphere-troposphere mixing. Such chemical tracer mixing features provide a useful tool to identify the origins of ice-supersaturated air parcels.

### 4.3. Influences of Mesoscale Uplifting, Small-Scale Waves, and Turbulence on Ice Microphysics

The dynamical conditions in RF04 and RF11 are further compared by using the in situ data of vertical wind speed and ice microphysical properties (Figures 7 and 8). The potential vorticity contours of  $\text{PVU}=2, 4,$  and  $8$  ( $1 \text{ PVU} = 10^{-6} \text{ K m}^2 \text{ kg}^{-1} \text{ s}^{-1}$ ) are used to illustrate the structure of dynamical tropopause, such as stratospheric intrusion (intrusion of  $\text{PVU}=2$  surface) and jet stream (large separation between  $\text{PVU}=2$  and  $\text{PVU}=8$  surfaces).

For times series of in situ vertical velocity in RF04 (Figure 7b), the horizontal segment ( $\sim 100$  km) of where ISS was observed (21:34:20–21:42:50 UTC) shows an average updraft of  $\sim 0.6$  m/s, consistent with the mesoscale uplifting in GOES 12 imagery referred from the cooling of cloud tops. In contrast, for RF11 (Figure 8b), the average vertical velocity for one horizontal segment ( $\sim 25$  km) of ISS observations (19:05:20–19:07:10 UTC) is  $\sim 0.08$  m/s,

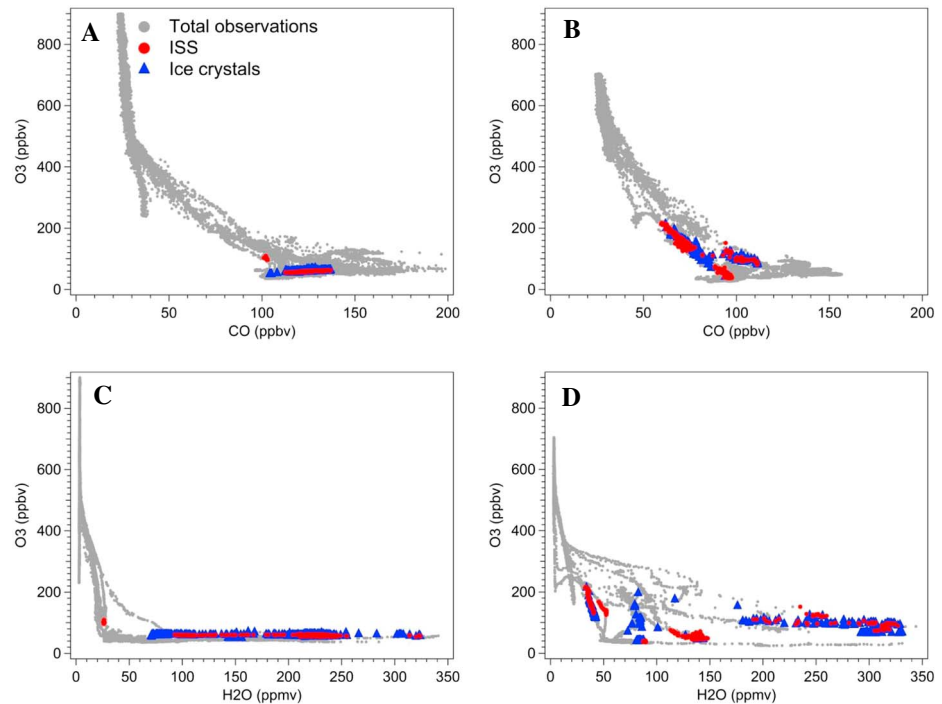


**Figure 6.** (a and b)  $O_3$ -CO and (c and d)  $O_3$ - $H_2O$  tracer-tracer correlations for (a and c) RF04 and (b and d) RF11. The red dots and blue triangles show the 1 Hz ISS and ice crystal observations in that flight, respectively. The grey color background shows all the observations in that flight at all temperatures.

In this work, we did not observe the strong anticorrelation between  $D_c$  and  $N_c$  values that was shown in previous simulations of ice nucleation [Gensch *et al.*, 2008; Krämer *et al.*, 2009]. This could be due to continuous uplifting, as reported by observational analyses [Diao *et al.*, 2013] and cloud modeling studies [Spichtinger and Gierens, 2009b], and therefore, ice crystal formation was not limited to a single nucleation event with a certain amount of water vapor over saturation. Another possible reason for the lack of anticorrelation between  $D_c$  and  $N_c$  could be due to the ice particle size range used in this analysis, since our quality control on 2DC probe filtered out ice particles  $< 100 \mu\text{m}$  and the SID\_2H probe measures up to  $50 \mu\text{m}$ . We note that the START08 flights do not have aerosol composition measurements; thus, we cannot investigate the roles of aerosol composition in contributing to the different ice crystal properties between RF04 and RF11. Future work is suggested to compare different meteorological conditions under similar aerosol compositions in order to separate the aerosol effects from the dynamical effects in the formation of cirrus clouds.

## 5. Composite Analyses of 15 Flights on ISS and Ice Crystal Spatial Distributions

### 5.1. Distributions of ISS and Ice Crystals in Tropopause and Jet Core Referenced Coordinate

We create a composite data set of START08 RF04–18 to systematically analyze the spatial distributions of ISS and ice crystals. Occurrence frequency distributions of 1 Hz ISS and ice crystals in the dynamical coordinates referenced to the tropopause and jet core are shown in Figures 9a and 9b, respectively. The occurrence frequency of ISS (or ice crystal) observations is calculated as the number of such observations normalized by the total number of 1 Hz aircraft observations (for  $T \leq -40^\circ\text{C}$ ) in each bin. The average profiles of tropopause height, potential temperature, and horizontal wind speed in Figure 9 are the same as Figure 1b. Because the sampling domain of the START08 campaign mostly targeted on the poleward side of the subtropical jet stream, the observations are almost exclusively around the extratropical tropopause rather than the tropical tropopause layer. Figure 9 shows that the occurrences of ISS and ice crystals are mostly limited to below the tropopause and exclusively below the +1 standard deviation of the tropopause height. For the relationship with jet core, high occurrence frequencies ( $\sim 0.4$ –1) of ISS and ice crystals are observed in a small region that is in the vicinity of the

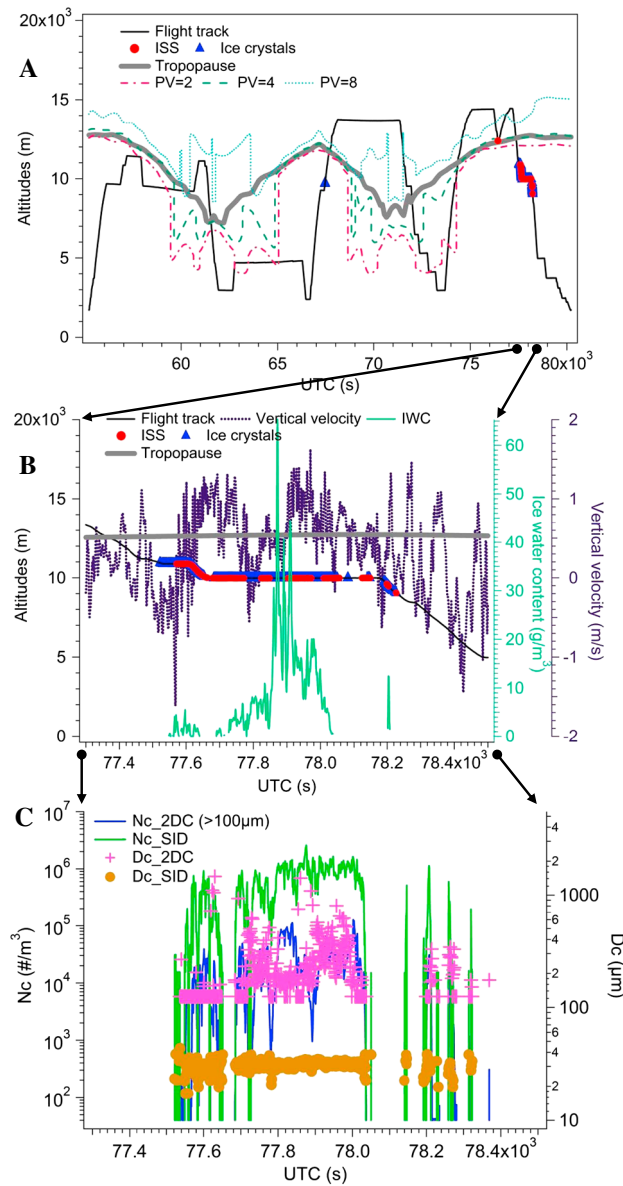


**Figure 7.** Time series analyses for RF04. (a) Vertical distributions of ISS and ice crystals with respect to thermal tropopause. The flight track and thermal tropopause are shown in solid black and grey lines, respectively; PVU = 2, 4, and 8 contours (red, green, and blue dotted lines, respectively) are used to illustrate the structure of dynamical tropopause. ISS and ice crystal observations at 1 Hz are shown in red solid circles and blue triangles, respectively. (b) Time series of vertical velocity (dashed purple) and ice water content (IWC, green solid line). (c) Time series of ice crystal concentrations (Nc, blue for 2DC and green for SID-2H) and volume-weighted mean diameter (Dc, pink for 2DC and yellow for SID-2H).

jet core (~300–500 km) on the cyclonic side, which may be a result of clear-air turbulence that generally wraps around the jet core on the cyclonic side along the PVU contours [Shapiro, 1976].

### 5.2. Comparison of ISS and Ice Crystal Distributions With Respect to Tropopause Height

To compare the vertical distributions between ISS and ice crystals, the probability distributions of (1) clear-sky ISS, (2) in-cloud ISS, and (3) ice crystals are separately plotted with respect to the thermal tropopause height (Figure 10a). As before, the occurrence frequency in each vertical bin is normalized by the total number of observations (at  $T \leq -40^\circ\text{C}$ ) inside that bin. Here the GFS tropopause level is shown with  $\pm 0.5$  km uncertainties (yellow stippling). The peak position of clear-sky ISS distribution is located at about 0.25 km above the tropopause, which is within the  $\pm 0.5$  km uncertainty of GFS thermal tropopause height. In contrast, the peak positions of in-cloud ISS and ice crystal distributions are located at lower altitudes with respect to the tropopause, i.e., around 2 to 6 km below the tropopause. The relatively lower altitudes of the peak occurrences of in-cloud ISS and ice crystals point to sedimentation of ice crystals during the lifetime of the cloud. These results are consistent with previous cloud simulations, which show that clear-sky ISS is generally located at the top level of the cirrus clouds and a deep layer of ice crystals extends up to ~6 km below the nucleation levels due to vertical mixing and sedimentation [Jensen *et al.*, 2013b]. We note that a small percentage (~5.4%) of the total ice crystal observations is located above the tropopause, but they almost exclusively (except 42 s) are within the 0.5 km uncertainty. A similar feature of ice

crystals located slightly above the tropopause has also been reported by Pan and Munchak [2011], but the authors commented that this feature may be entirely due to the uncertainties in tropopause height determination.

Because the magnitude of RHi is an important factor in ice crystal formation, we also analyze the occurrence frequency distributions for different ranges of RHi (>100%, >110%, >120%, and >130%) with respect to the

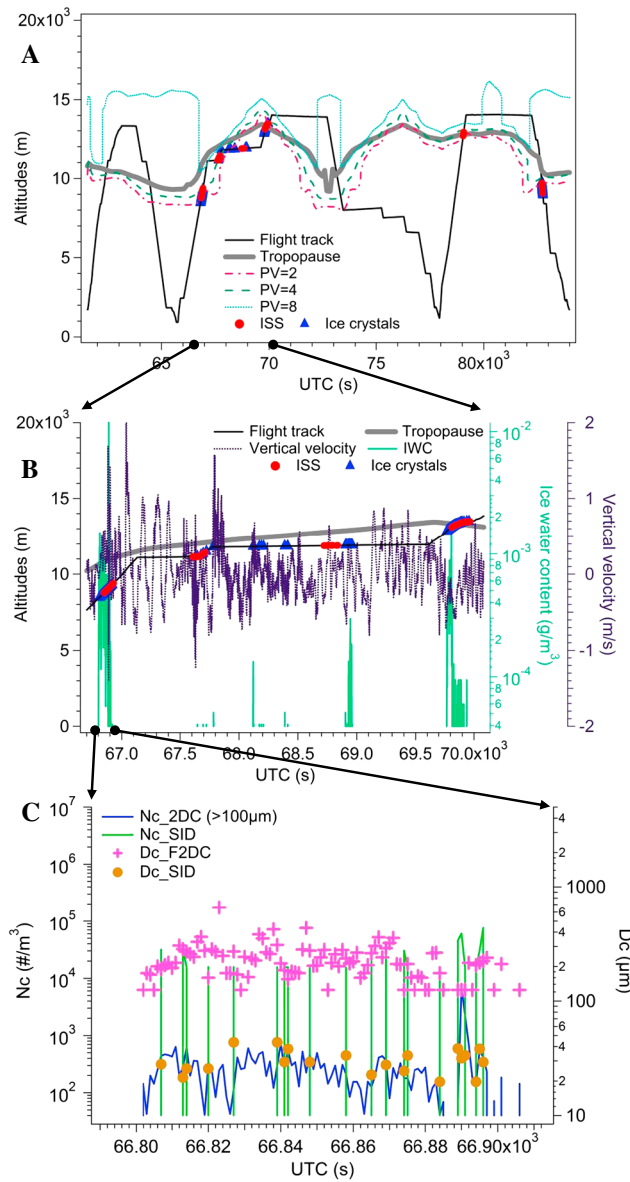


Figure 8. Similar to Figure 7, time series analyses for RF11.

thermal tropopause (Figure 10b). The probability at each bin is calculated by the number of ISS observations (both clear-sky and in-cloud conditions) normalized by the total number of observations at  $T \leq -40^\circ\text{C}$  inside that bin. Similar to ISS distributions in Figure 10a, two main peaks of ISS distributions are observed: one near the tropopause and the other at  $\sim 1\text{ km}$  below. We note that when using the  $1\text{ km}$  vertical bin size, the two peaks of the frequency distribution of  $\text{RHi} > 100\%$  still exist. To determine whether such two-peak feature is due to the limited sample size of the current data set requires more intensive observations around the extratropical tropopause. As the magnitudes of  $\text{RHi}$  increase, the probabilities of ISS observations decrease about 2 orders of magnitude, from  $\sim 0.01\text{--}0.11$  ( $\text{RHi} > 100\%$ ) to  $\sim 0.0003\text{--}0.004$  ( $\text{RHi} > 130\%$ ).

The PDF of  $\text{RHi}$  at  $T \leq -40^\circ\text{C}$  is shown in Figure 10c, and the maximum  $\text{RHi}$  observed in this data set is below  $150\%$ . The PDF of  $\text{RHi}$  for the in-cloud condition peaks around  $100\%$ . On the other hand, the PDF of  $\text{RHi}$  for the clear-sky condition peaks around  $5\text{--}10\%$  due to the frequent sampling in the lower stratosphere. We note that the lack of observations at  $\text{RHi} > 150\%$  could be due to that only a thin layer at the cirrus cloud top reaches  $\text{RHi} > 150\%$ , while the rest of  $\text{RHi}$  vertical profile is generally below  $150\%$ , according to the model simulations of Spichtinger and Gierens [2009b].

### 5.3. Distributions of ISS and Ice Crystals on the Cyclonic and Anticyclonic Sides of the Jet Core

The jet core generally marks the boundary between the extratropical cyclonic and anticyclonic systems. To quantify the occurrence frequencies of ISS and ice crystals between the anticyclonic and cyclonic sides, their occurrence frequency distributions with respect to the jet core are shown in Figure 11. The probabilities of ISS and ice crystals within each bin are normalized by the total number of observations ( $T \leq -40^\circ\text{C}$ ) in that bin. The peak occurrence frequencies of ISS and ice crystals are located at  $\sim 5$  arc degrees (i.e.,  $550\text{ km}$ ) from the jet core on both the cyclonic and anticyclonic sides. For observations within  $\sim 800\text{ km}$  of the jet ( $> 7000$  of  $1\text{ Hz}$  observations in each bin), the average probabilities of observing ISS and ice crystals on the anticyclonic side are  $\sim 1.6$  and  $2.0$  times of those on the cyclonic side, respectively. We note that these ratios between the cyclonic and anticyclonic sides are subject to the possible biases in the sampling between the two sides. To derive the climatological ratios of ISS and ice crystal distributions between the two sides, one would need 3-D sampling with longer time span, such as remote sensing observations.

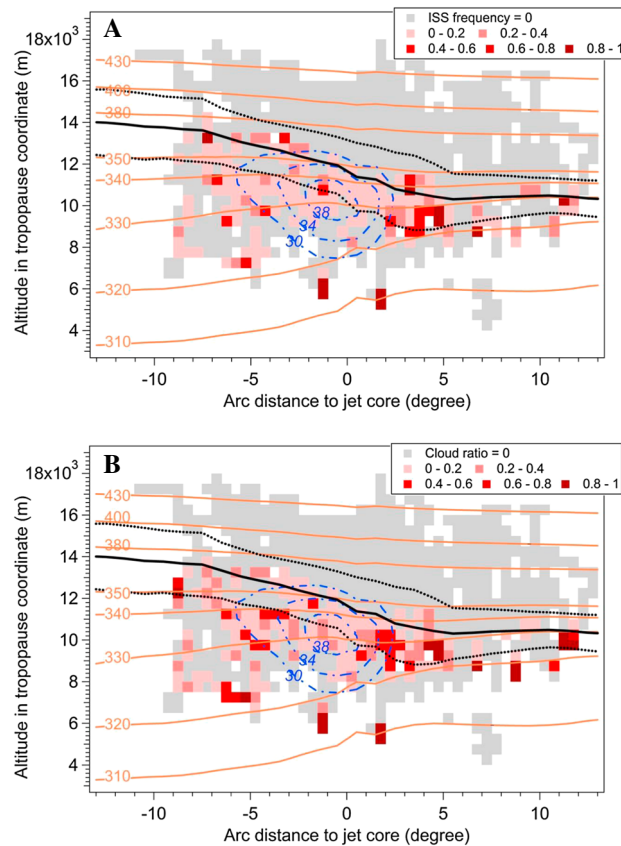


**Figure 9.** ISS and ice crystals distributions in the tropopause relative coordinate (vertical) and jet core coordinate (horizontal) for START08 RF04–18 at  $T \leq -40^\circ\text{C}$ . The average atmospheric profiles, as well as the ordinate and abscissa for flight observations, are the same as those in Figure 1b. (a) The occurrence frequency of ISS observations are calculated for each bin ( $500\text{ m} \times 0.5^\circ$ ), normalized by the total number of observations at  $T \leq -40^\circ\text{C}$  in that bin. The grey colors show where ISS occurrence frequency = 0; the red colors from light to dark show five ranges of ISS occurrence frequencies at  $0^+ - 0.2$ ,  $0.2 - 0.4$ ,  $0.4 - 0.6$ ,  $0.6 - 0.8$ , and  $0.8 - 1$  ranges. (b) Similar to Figure 9a but for ice crystal occurrence frequency distribution.

The variation in the vertical distributions for the five phases is quantified in Figure 13. The occurrence frequency of each phase is calculated by the number of 1 Hz observations for each phase normalized by the total 1 Hz observations (at  $T \leq -40^\circ\text{C}$ ) in that bin. We note that the phase of clear-sky ISSRs (as a consecutive region) in Figures 12a and 13 is different from the 1 Hz clear-sky ISS (at 1 s scale) observations in Figure 10a, since the 1 Hz clear-sky observations also occur in phases 2–4.

For observations on both the cyclonic and anticyclonic sides (Figure 13a), the occurrence frequency distribution of the nucleation phase (red dotted line) peaks at  $\sim 0.25\text{ km}$  above the NCEP GFS thermal tropopause and within its  $0.5\text{ km}$  uncertainty. In contrast, the early growth (dashed blue line) and later growth (dotted-dashed green line) phases peak at  $\sim 2\text{ km}$  and  $\sim 6\text{ km}$  below the thermal tropopause, respectively. These results show that during the evolution of cirrus clouds, the vertical positions of their peak occurrence frequencies move downward with respect to thermal tropopause. In addition, the ice crystals in sedimentation/sublimation (light blue line) show several peaks in their vertical frequency distribution, which is likely due to sedimentation and sublimation happening throughout the evolution of cirrus clouds and at multiple layers within the clouds. These observed vertical variations during cirrus cloud evolution agree with the previous cloud simulations, which showed that the ice crystals could extend to  $\sim 2\text{--}5\text{ km}$  below the nucleation sites [Spichtinger and Gierens, 2009b; Jensen et al., 2013b].

## 6. An Evolutionary View of Cirrus Clouds' Vertical Distributions

### 6.1. Distributions of Five Evolution Phases of Cirrus Clouds in Relation to the Thermal Tropopause

To provide an evolutionary view of ISS locations with respect to the thermal tropopause, we analyze the ISSR+ICR samples of five evolution phases using the method of Diao et al. [2013], i.e., clear-sky ISSRs (phase 1), ISSRs with ice nucleation (phase 2), ISSRs intersected with ICRs at early growth stage (phase 3), ISSRs embedded inside large ICRs at later growth stage (phase 4), and ICRs in sedimentation/ sublimation without ISS (phase 5). These five phases are represented in Figures 12a–12e, respectively. In Figure 12, the tropopause relative coordinate is the same as that in Figure 9. The green triangles represent the 1 Hz observations for the ISSR+ICR samples. The earlier evolution phases, i.e., clear-sky ISSRs and ice crystal nucleation, occur in closer proximity to the tropopause than the later phases. In particular, the sedimentation/sublimation phase has the widest range of vertical distribution compared with other phases. We note that almost all ( $\sim 99.6\%$ ) ice crystals are located below the  $0.5\text{ km}$  uncertainty of GFS tropopause and the nucleation phase samples above  $0.5\text{ km}$  of the tropopause are actually the clear-sky segments of the nucleation phase.

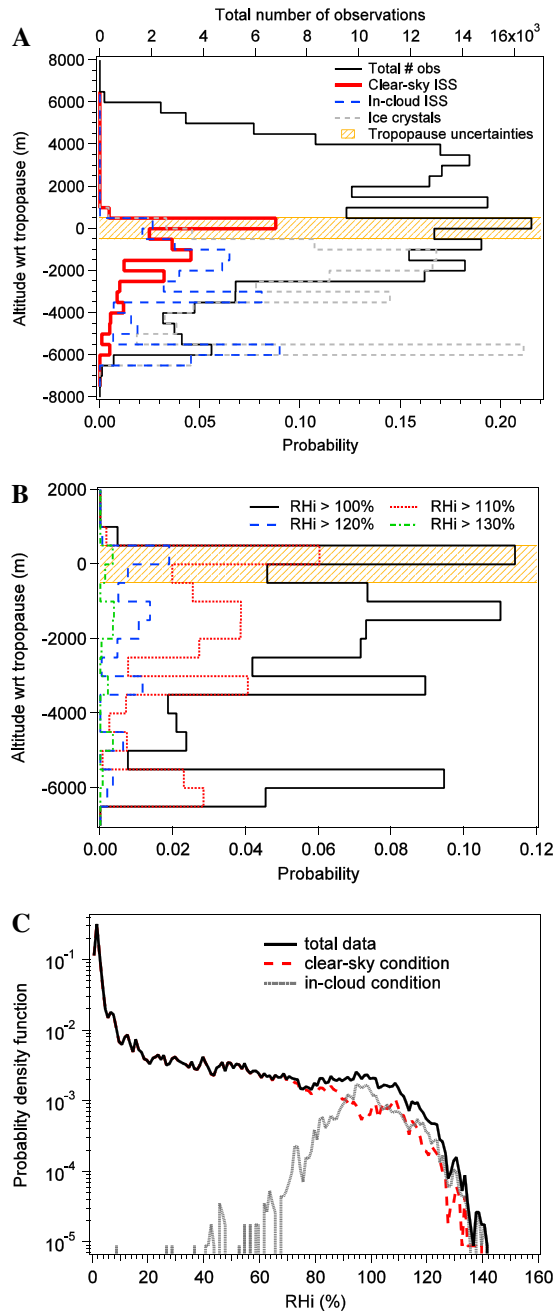


**Figure 10.** Vertical occurrence frequency distributions of ISS and ice crystals with respect to thermal tropopause. (a) The probabilities of ISS observations in clear-sky (red solid line) and in-cloud (blue dashed line) conditions and the probabilities of ice crystal observations (grey dotted line) are shown in each layer with respect to the thermal tropopause height. The distribution of total number of observations is shown in black solid line (top abscissa). (b) Similar to Figure 10a but for ISS at different RH magnitudes: RHi > 100% (black), RHi > 110% (red dotted), RHi > 120% (blue dashed), and RHi > 130% (green dot-dashed). The probability in each bin (binned by 0.5 km) is normalized by the total number of observations at  $T \leq -40^\circ\text{C}$  in that bin. The yellow stippling shows the GFS tropopause uncertainties of  $\pm 0.5$  km. (c) Probability density function of RHi at  $T \leq -40^\circ\text{C}$  for total observations, clear-sky, and in-cloud conditions.

The observed peak occurrence frequency of ice nucleation around the thermal tropopause is likely due to a combination of reasons, including the abrupt changes of temperature and humidity across the tropopause, as well as the frequent occurrence of clear-air turbulence around the jet stream. As the saturation vapor pressure increases exponentially with temperature according to the Clausius-Clapeyron equation, a small perturbation of the moisture or temperature field near the tropopause would be more likely to produce high RHi than at lower levels. In fact, our findings on the distributions of cirrus evolution phases are consistent with previous lidar observations of cirrus cloud distributions over France in Noël and Haefelin [2007]. The authors reported that the peak frequency of occurrence of cirrus cloud top is close to the tropopause and the frequency of occurrence of cirrus cloud base peaks at two locations: 1–1.5 km and 3–3.5 km below the tropopause.

When comparing the vertical distributions of five cirrus evolution phases between the anticyclonic side (Figure 13b) and cyclonic side (Figure 13c), the peak occurrence frequencies of the nucleation and early growth phases occur around the same altitude relative to the tropopause on both sides. On the other hand, for the later growth and sedimentation/sublimation phases, their peak occurrence frequencies are located closer to the tropopause on the cyclonic side (~2 km below the tropopause) than the anticyclonic side (~6 km below the tropopause). To determine whether such a feature is due to the different ice particle fall speed between the two sides requires future observations targeting the vertical distribution of ice crystals in cirrus layers.

Another main difference in the vertical distributions between the two sides is that the peak occurrence frequencies of nucleation and early growth phases are ~1.5 and 1.2 times higher on the anticyclonic side than the cyclonic side, respectively. The slightly higher frequencies of ISS on the anticyclonic side of the jet agree with the previous ECMWF simulations, which show more ISSRs associated with anticyclonic systems than cyclonic systems over Europe (similar latitudes to START08) [Gierens and Brinkop, 2012]. In addition, remote sensing analyses showed that higher occurrences of cirrus clouds happen on the

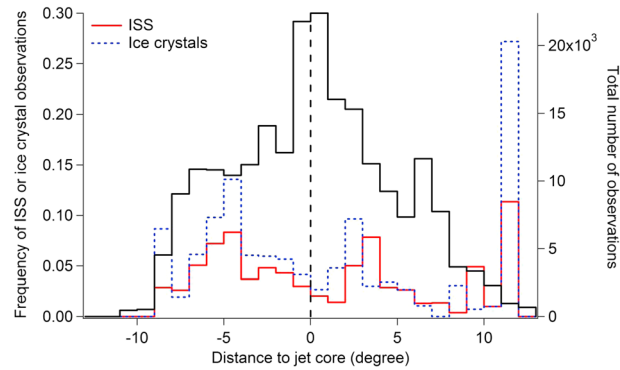


**Figure 11.** Distributions of ISS and ice crystals on the anticyclonic (negative abscissa) and cyclonic sides (positive abscissa) of the jet core for START08 RF04–18 at  $T \leq -40^\circ\text{C}$ . The abscissa is similar to Figure 1, representing the arc distance (in degree) from observations to jet core. The dashed line is to highlight the location of jet core. Occurrence frequency distributions of ISS (red solid line) and ice crystals (blue dotted line) at each horizontal distance bin (binned by  $1^\circ$ ) are shown on the left ordinate. Total number of observations ( $T \leq -40^\circ\text{C}$ ) in each bin is shown on the right ordinate (black solid line).

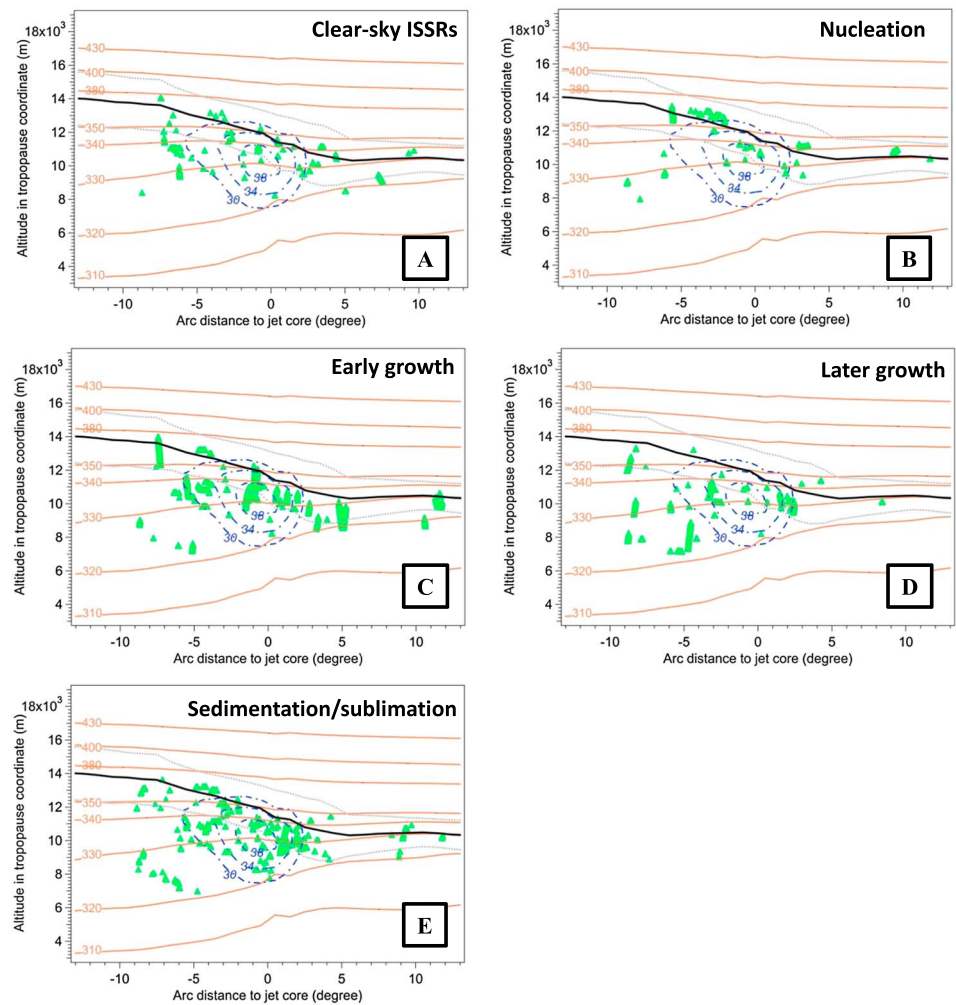


**Figure 12.** Distributions of the five evolution phases of cirrus clouds in the dynamical coordinates in thermal tropopause relative coordinate (vertical) and jet core coordinate (horizontal) for START08 RF04–18. The coordinate system is the same as Figure 1b. Observations of five evolution phases are shown as green triangles in (a) clear-sky ISSRs, (b) ice crystal nucleation phase, (c) early growth, (d) later growth, and (e) sedimentation/sublimation. We note that the clear-sky ISSRs (a consecutive region without ice crystals) in Figure 12a are different from the clear-sky ISS (1 s scale without ice crystals) in Figure 10a.

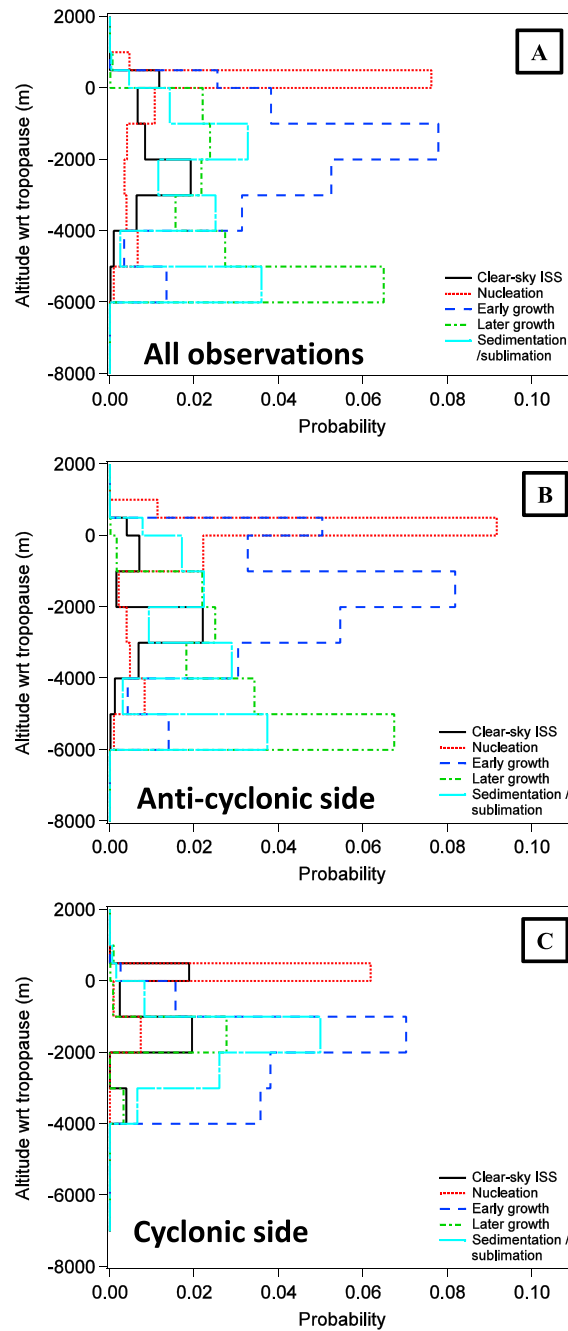


**Figure 13.** Occurrence frequency distributions of 1 Hz observations for five evolution phases with respect to thermal tropopause. (a–c) Observations at  $T \leq -40^\circ\text{C}$  for the total data set, anticyclonic side, and cyclonic side, respectively. Phases 1–5 are shown in black solid, red dotted, dark blue dashed, green dot-dashed, and light blue dot-dashed lines, respectively. The occurrence frequencies are normalized by total number of observations at  $T \leq -40^\circ\text{C}$  in each bin (shown in Figure 10a). Note that we use 0.5 km bins above the tropopause and 1 km bins below the tropopause.

that is,  $\text{O}_3 = n_0 + n_1 \times \text{CO}$ , where  $n_0 = 44.1 \pm 0.1$  and  $n_1 = 0.088 \pm 0.001$ . The horizontal dashed black lines represent  $\pm 3\sigma_{r2}$  ( $\sigma_{r2}$  is the standard deviation of the residuals of the linear fit), where  $\sigma_{r2} = 10.9$  ppbv. The light blue line represents the border for the transition layer in tracer space, where the two end points of

anticyclonic systems over the U.S. and many opaque cirrus occur in the ridges of Rossby waves and on the anticyclonic side of the jet [Wylie, 2002]. In contrast, at the troughs of Rossby waves and on the cyclonic side of the jet, the prevailing condition is clear sky.

We caution that there are several limitations in using this method to convert the Eulerian observations into an evolutionary view. For example, new ice crystals formed heterogeneously near saturation may not be captured by the nucleation phase, since ISS is required for its definition. In addition, the transport history of ice crystals has not been addressed by the current analysis. More future work is suggested to use model simulations with 3-D structure of cirrus clouds to analyze the vertical distributions of cirrus clouds in an evolutionary view.

### 6.2. Distributions of Five Cirrus Evolution Phases in the $\text{O}_3$ -CO Coordinate

We use tracer-tracer relationships to analyze the distributions of the five evolution phases of cirrus clouds with respect to the extratropical chemical tropopause transition layer. Figure 14 shows the scatterplot of  $\text{O}_3$ -CO tracer-tracer relationships, where the grey background represents observed domain at all temperature ranges. The red markers in Figures 14a–14e represent the 1 Hz observations that belong to each of the five evolution phases. We define the regions of extratropical stratosphere branch, troposphere branch, and transition layer following the previous definitions in Pan et al. [2004], with new fittings applied to the START08 data. The vertical solid black line represents a polynomial fit to the chemical stratosphere branch ( $\text{CO} < 35$  ppbv); that is,  $\text{CO} = m_0 + m_1 \times \text{O}_3 + m_2 \times \text{O}_3^2$ , where  $m_0 = 46.8 \pm 0.08$ ,  $m_1 = -0.0433 \pm 0.0003$ , and  $m_2 = 1.82\text{e-}05 \pm 2.01\text{e-}07$ , with both CO and  $\text{O}_3$  in units of ppbv. The vertical dashed black lines represent  $\pm 3\sigma_{r1}$  ( $\sigma_{r1}$  is the standard deviation of the residuals of the poly3 fit), where  $\sigma_{r1} = 1.49$  ppbv. In addition, the horizontal solid black line represents the linear fit to the chemical troposphere branch ( $\text{O}_3 < 70$  ppbv);

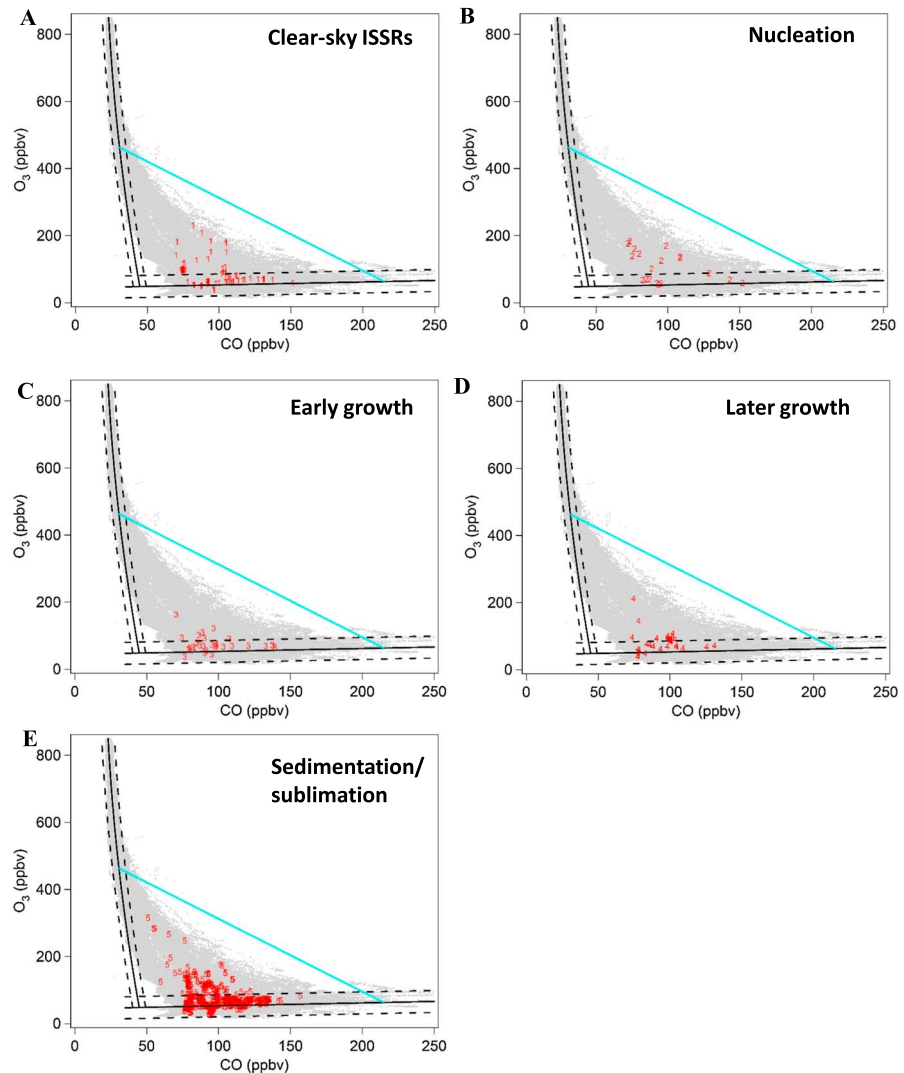


**Figure 14.** Distributions of five cirrus evolution phases in chemical tracer coordinate of  $O_3$ -CO for RF04-18. (a-e) Observations of five phases (red markers) are the same as those in Figure 12. The grey background represents observations at all temperature ranges. The figures zoom into  $O_3 < 850$  ppbv and  $CO < 250$  ppbv for a clearer view of the five phases. The vertical and horizontal black solid lines represent the fits for extratropical stratospheric branch and tropospheric branch in the tracer space, respectively. The  $\pm 3\sigma$  of the fits are shown in dashed black lines. On the left of the vertical fit is the stratospheric branch, below the horizontal fit is the tropospheric branch, and in between is the transition layer. The end points of the light blue line mark the border of where a significant number of data points ( $>10\%$ ) start to deviate from the compact relationship ( $\pm 3\sigma$  of the fits). These end points are  $CO = 28$  ppbv and  $O_3 = 503$  ppbv for the stratosphere branch and  $CO = 215$  ppbv and  $O_3 = 63$  ppbv for the troposphere branch.

the light blue line represent the positions where a significant amount of data ( $>10\%$ ) start to deviate from the compact fits for each reservoir (within  $+3\sigma$ ) for chemical troposphere and stratosphere.

In the tracer-tracer coordinate, the ISSRs and ICRs have been observed in both the transition layer (typically located at  $\sim 8$ - $13$  km in START08 with a depth around  $0.5$ - $1.5$  km) and tropospheric branch. No ISS or ice crystals were observed in the stratospheric branch in tracer space. To quantify the variations in the distributions of five phases, Table 3 shows the ratio of each phase in the transition layer and the tropospheric branch. For earlier phases of clear-sky ISSRs and ice crystal nucleation,  $69\%$  and  $85\%$  of the samples are located in the transition layer, respectively. In contrast, the later phases occur mostly ( $>80\%$ ) in the chemical tropospheric branch. These analyses in the chemical tracer coordinate are consistent with those in the dynamical coordinates, as they both show descending locations of ISSRs and ICRs during the progression of the five evolution phases.

**Table 3.** Ratios of Five ISSR+ICR Evolution Phases Inside the Extratropical Chemical Transition Layer and the Tropospheric Branch Below the Transition Layer

Ratio of Each Phase	Clear-Sky ISSRs	Nucleation	Early Growth	Later Growth	Sedimentation/Sublimation
In transition layer	0.69	0.85	0.17	0.12	0.12
Below transition layer	0.31	0.15	0.83	0.88	0.88

## 7. Implications for Cirrus Cloud Simulations

Based on the observations of START08 campaign over the North American continent, two dynamical regimes are found to be involved with ISS and ice crystal formation, i.e., (1) mesoscale uplifting and (2) small-scale waves and turbulence. These two regimes were associated with different scales of dynamics (mesoscale versus small scale) and with mixing of different air masses. The IWC and  $N_c$  values were found to be very different ( $\sim 1$ – $2$  orders of magnitude differences) between the two situations, which points to the complexity of comparing in situ observations of IWC and  $N_c$  with cloud modeling results. Our case studies suggest that ISS and ice crystal formation does not always require upward motion on the large scale, since smaller-scale uplift can also be a contributor. Due to the lack of aerosol composition measurements, more future measurements are suggested to separate the aerosol factors from the dynamical influences.

Two types of coordinates (i.e., dynamical coordinates and chemical tracer coordinates) are used to analyze ISS and ice crystal distributions in relation to upper tropospheric dynamics. The combination of these two coordinates provides a comprehensive view of both large-scale dynamical background and distinct air mass compositions on the microscale. Future studies are suggested to conduct comparative analyses between in situ observations and cloud-resolving model simulations based on these two sets of coordinates. For example, analyzing the tracer-tracer correlation based on the passive tracers released in a cloud-resolving model [e.g., *Bryan and Morrison, 2012*] can help assess the formation mechanisms of cirrus clouds in models.

For the vertical distributions of cirrus clouds, our results show that the predominant locations of earlier phases of cirrus clouds (clear-sky ISSRs and nucleation phases) are located near the thermal tropopause, while those of latter phases are located at  $\sim 2$ – $6$  km below the tropopause. These results suggest that excluding ISS in model simulations would lead to more artificial ice crystals and less water vapor from around the tropopause to  $\sim 6$  km below the tropopause. In addition, the maximum underestimation of water vapor would happen near the thermal tropopause. Such underestimation can have large impacts on the atmospheric radiative forcing due to its high sensitivity to water vapor perturbations around the tropopause. Thus, including subgrid-scale variabilities of ISS and ice crystals may help to improve the simulations of cirrus cloud radiative forcing throughout the cloud lifetime. Future studies are suggested to evaluate cloud model results for their representations of five evolution phases. In addition, quantifying the perturbations in atmospheric radiative forcing caused by ISS exclusion in each evolution phase requires further study.

Due to the spatial and temporal limitations of in situ measurements, this work only provides two case studies, i.e., mesoscale uplifting versus small-scale waves and turbulence, in addition to the composite data set of 15 flights. More future case studies are suggested to examine other dynamical conditions, such as lee waves and deep convection, for their influences on cirrus cloud formation. The current data set only has a few cases (RF06 and RF12) where deep convection has been identified [*Homeyer et al., 2011*], and removing the regions with strong updraft and downdraft does not influence our conclusions on the distributions of ISS and ice crystals. The GFS data used in this study are 6 hourly, which may not sufficiently resolve rapid changes in the meteorological background (e.g., frontal passages). Future analyses using higher-resolution GFS data would help to resolve the relationship between frontal systems and ISS formation. Additional statistical analyses are needed to quantify the contribution of different types of dynamical conditions to ISS and ice crystal formation on regional and global scales. Furthermore, the observations in this work are limited to the Northern Hemisphere midlatitudes, which may or may not be applicable to other regions. Expanding this analysis to other regions will likely rely on remote sensing techniques with greater coverage. In particular, as the sampling domains in this study were focused around the extratropical thermal tropopause, more analyses are needed to address these features in the tropical tropopause layer.

**Acknowledgments**

We gratefully acknowledge funding for field support and data analyses from the following sources: ATM-0840732 for VCSEL hygrometer in the START08 campaign. M.D. gratefully acknowledges support from the NASA Earth and Space Science Graduate Fellowship (NNX09AO51H) and the National Center for Atmospheric Research (NCAR) Advanced Study Program postdoctoral fellowship. The National Center for Atmospheric Research is sponsored by the National Science Foundation. We appreciate the efforts of NCAR EOL flight, technical, and mechanical crews during START08 campaign. We acknowledge the support from A.J. Heymsfield for SID-2H probe; D.C. Rogers and C.J. Webster for 2DC probe; M.A. Zondlo, S.P. Beaton, and P. Romashkin for the support of VCSEL hygrometer; and T. Campos for the support of CO and O<sub>3</sub> measurements by NCAR dual-beam ultraviolet absorption photometer and chemiluminescent reaction detector. We also appreciate helpful discussions with W.A. Cooper, R. Carbone, R.B. Friesen, D. Lenschow, E. Jensen, and U. Schumann. All data used in this study are free and publicly available. START08 aircraft observations were obtained at <http://data.eol.ucar.edu/codiac/projs?START08/> and NCEP-GFS analyses at <http://nomads.nccdc.noaa.gov/>.

**References**

- Birner, T., A. Dörnbrack, and U. Schumann (2002), How sharp is the tropopause at midlatitudes?, *Geophys. Res. Lett.*, *29*(14), 1700, doi:10.1029/2002GL015142.
- Brioude, J., J.-P. Cammas, O. R. Cooper, and P. Nedelec (2008), Characterization of the composition, structure, and seasonal variation of the mixing layer above the extratropical tropopause as revealed by MOZIC measurements, *J. Geophys. Res.*, *113*, D00B01, doi:10.1029/2007JD009184.
- Brown, P. R. A., and P. N. Francis (1995), Improved measurements of the ice water content in cirrus using a total-water probe, *J. Atmos. Oceanic Technol.*, *12*(2), 410–414, doi:10.1175/1520-0426(1995)012<0410:MOTIW>2.0.CO;2.
- Bryan, G. H., and H. Morrison (2012), Sensitivity of a simulated squall line to horizontal resolution and parameterization of microphysics, *Mon. Weather Rev.*, *140*(1), 202–225, doi:10.1175/MWR-D-11-00046.1.
- Cotton, R., S. Osborne, Z. Ulanowski, E. Hirst, P. H. Kaye, and R. S. Greenaway (2010), The ability of the Small Ice Detector (SID-2) to characterize cloud particle and aerosol morphologies obtained during flights of the FAAM BAe-146 research aircraft, *J. Atmos. Oceanic Technol.*, *27*(2), 290–303, doi:10.1175/2009JTECHA1282.1.
- Cziczo, D. J., K. D. Froyd, C. Hoese, E. J. Jensen, M. Diao, M. A. Zondlo, J. B. Smith, C. H. Twohy, and D. M. Murphy (2013), Clarifying the dominant sources and mechanisms of cirrus cloud formation, *Science*, *340*(6138), 1320–1324, doi:10.1126/science.1234145.
- Diao, M., M. A. Zondlo, A. J. Heymsfield, S. P. Beaton, and D. C. Rogers (2013), Evolution of ice crystal regions on the microscale based on in situ observations, *Geophys. Res. Lett.*, *40*, 3473–3478, doi:10.1002/grl.50665.
- Diao, M., M. A. Zondlo, A. J. Heymsfield, L. M. Avallone, M. E. Paige, S. P. Beaton, T. Campos, and D. C. Rogers (2014a), Cloud-scale ice-supersaturated regions spatially correlate with high water vapor heterogeneities, *Atmos. Chem. Phys.*, *14*, 1–18, doi:10.5194/acp-14-1-2014.
- Diao, M., M. A. Zondlo, A. J. Heymsfield, and S. P. Beaton (2014b), Hemispheric comparison of cirrus cloud evolution using in situ measurements in HIAPER Pole-to-Pole Observations, *Geophys. Res. Lett.*, *41*, 4090–4099, doi:10.1002/2014GL059873.
- Fischer, H., F. G. Wienhold, P. Hoor, O. Bujok, C. Schiller, P. Siegmund, M. Ambaum, H. A. Scheer, and J. Lelieveld (2000), Tracer correlations in the northern high latitude lowermost stratosphere: Influence of cross-tropopause mass exchange, *Geophys. Res. Lett.*, *27*(1), 97–100, doi:10.1029/1999GL010879.
- Follette-Cook, M. B., R. D. Hudson, and G. E. Nedoluha (2009), Classification of Northern Hemisphere stratospheric ozone and water vapor profiles by meteorological regime, *Atmos. Chem. Phys.*, *9*(16), 5989–6003, doi:10.5194/acp-9-5989-2009.
- Fusina, F., and P. Spichtinger (2010), Cirrus clouds triggered by radiation, a multiscale phenomenon, *Atmos. Chem. Phys.*, *10*(11), 5179–5190, doi:10.5194/acp-10-5179-2010.
- Fusina, F., P. Spichtinger, and U. Lohmann (2007), Impact of ice supersaturated regions and thin cirrus on radiation in the midlatitudes, *J. Geophys. Res.*, *112*, D24514, doi:10.1029/2007JD008449.
- Gensch, I. V., et al. (2008), Supersaturations, microphysics and nitric acid partitioning in a cold cirrus cloud observed during CR-AVE 2006: An observation–modelling intercomparison study, *Environ. Res. Lett.*, *3*(3), 035003, doi:10.1088/1748-9326/3/3/035003.
- Gerbig, C., S. Schmitgen, D. Kley, A. Volz-Thomas, K. Dewey, and D. Haaks (1999), An improved fast-response vacuum-UV resonance fluorescence CO instrument, *J. Geophys. Res.*, *104*(D1), 1699–1704, doi:10.1029/1998JD100031.
- Gottelman, A., E. J. Fetzer, A. Eldering, and F. W. Irion (2006), The global distribution of supersaturation in the upper troposphere from the Atmospheric Infrared Sounder, *J. Clim.*, *19*(23), 6089–6103, doi:10.1175/JCLI3955.1.
- Gottelman, A., X. Liu, D. Barahona, U. Lohmann, and C. Chen (2012), Climate impacts of ice nucleation, *J. Geophys. Res.*, *117*, D20201, doi:10.1029/2012JD017950.
- Gierens, K., and S. Brinkop (2012), Dynamical characteristics of ice supersaturated regions, *Atmos. Chem. Phys.*, *12*(24), 11,933–11,942, doi:10.5194/acp-12-11933-2012.
- Hartmann, D. L., J. R. Holton, and Q. Fu (2001), The heat balance of the tropical tropopause, cirrus, and stratospheric dehydration, *Geophys. Res. Lett.*, *28*(10), 1969–1972, doi:10.1029/2000GL012833.
- Homeyer, C. R., K. P. Bowman, L. L. Pan, M. A. Zondlo, and J. F. Bresch (2011), Convective injection into stratospheric intrusions, *J. Geophys. Res.*, *116*, D23304, doi:10.1029/2011JD016724.
- Hudson, R. D., A. D. Frolov, M. F. Andrade, and M. B. Follette (2003), The total ozone field separated into meteorological regimes. Part I: Defining the regimes, *J. Atmos. Sci.*, *60*(14), 1669–1677, doi:10.1175/1520-0469(2003)060<1669:TTOFSI>2.0.CO;2.
- Jaeger, E. B., and M. Sprenger (2007), A Northern Hemispheric climatology of indices for clear air turbulence in the tropopause region derived from ERA40 reanalysis data, *J. Geophys. Res.*, *112*, D20106, doi:10.1029/2006JD008189.
- Jensen, E. J., G. Diskin, R. P. Lawson, S. Lance, T. P. Bui, D. Hlavka, M. McGill, L. Pfister, O. B. Toon, and R. Gao (2013a), Ice nucleation and dehydration in the tropical tropopause layer, *Proc. Natl. Acad. Sci. U.S.A.*, *110*(6), 2041–2046, doi:10.1073/pnas.1217104110.
- Jensen, E. J., R. P. Lawson, J. W. Bergman, L. Pfister, T. P. Bui, and C. G. Schmitt (2013b), Physical processes controlling ice concentrations in synoptically forced, midlatitude cirrus, *J. Geophys. Res. Atmos.*, *118*, 5348–5360, doi:10.1002/jgrd.50421.
- Johnson, A., S. Lasher-Trapp, A. Bansemer, Z. Ulanowski, and A. J. Heymsfield (2014), Difficulties in early ice detection with the Small Ice Detector-2 HIAPER (SID-2H) in maritime cumuli, *J. Atmos. Oceanic Technol.*, *31*(6), 1263–1275, doi:10.1175/JTECH-D-13-00079.1.
- Kahn, B. H., C. K. Liang, A. Eldering, A. Gottelman, Q. Yue, and K. N. Liou (2008), Tropical thin cirrus and relative humidity observed by the Atmospheric Infrared Sounder, *Atmos. Chem. Phys.*, *8*(6), 1501–1518, doi:10.5194/acp-8-1501-2008.
- Kahn, B. H., A. Gottelman, E. J. Fetzer, A. Eldering, and C. K. Liang (2009), Cloudy and clear-sky relative humidity in the upper troposphere observed by the A-train, *J. Geophys. Res.*, *114*, D00H02, doi:10.1029/2009JD011738.
- Kahn, B. H., et al. (2014), The Atmospheric Infrared Sounder version 6 cloud products, *Atmos. Chem. Phys.*, *14*(1), 399–426, doi:10.5194/acp-14-399-2014.
- Kärcher, B., and U. Burkhardt (2008), A cirrus cloud scheme for general circulation models, *Q. J. R. Meteorol. Soc.*, *134*(635), 1439–1461, doi:10.1002/qj.301.
- Kärcher, B., and P. Spichtinger (2009), Cloud-controlling factors of cirrus, in *Clouds in the Perturbed Climate System*, edited by J. Heintzenberg and R. J. Charlson, pp. 173–196, MIT Press, Cambridge, Mass.
- Keyser, D., and M. A. Shapiro (1986), A review of the structure and dynamics of upper-level frontal zones, *Mon. Weather Rev.*, *114*(2), 452–499, doi:10.1175/1520-0493(1986)114<0452:AROTSA>2.0.CO;2.
- Konopka, P., and L. L. Pan (2012), On the mixing-driven formation of the extratropical transition layer (ExTL), *J. Geophys. Res.*, *117*, D18301, doi:10.1029/2012JD017876.
- Krämer, M., et al. (2009), Ice supersaturations and cirrus cloud crystal numbers, *Atmos. Chem. Phys.*, *9*(11), 3505–3522.
- Lamquin, N., C. J. Stubenrauch, K. Gierens, U. Burkhardt, and H. Smit (2012), A global climatology of upper-tropospheric ice supersaturation occurrence inferred from the Atmospheric Infrared Sounder calibrated by MOZIC, *Atmos. Chem. Phys.*, *12*(1), 381–405, doi:10.5194/acp-12-381-2012.

- Liou, K. N. (1992), *Radiation and Cloud Processes in the Atmosphere*, pp. 255–339, Oxford Univ. Press, New York.
- Manney, G. L., et al. (2011), Jet characterization in the upper troposphere/lower stratosphere (UTLS): Applications to climatology and transport studies, *Atmos. Chem. Phys.*, *11*(12), 6115–6137, doi:10.5194/acp-11-6115-2011.
- Massie, S. T., J. Gille, C. Craig, R. Khosravi, J. Barnett, W. Read, and D. Winker (2010), HIRDLS and CALIPSO observations of tropical cirrus, *J. Geophys. Res.*, *115*, D00H11, doi:10.1029/2009JD012100.
- Noël, V., and M. Haefelin (2007), Midlatitude cirrus clouds and multiple tropopauses from a 2002–2006 climatology over the SIRTA observatory, *J. Geophys. Res.*, *112*, D13206, doi:10.1029/2006JD007753.
- Ovarlez, J., J. F. Gayet, K. Gierens, J. Strom, H. Ovarlez, F. Auriol, R. Busen, and U. Schumann (2002), Water vapour measurements inside cirrus clouds in Northern and Southern Hemispheres during INCA, *Geophys. Res. Lett.*, *29*(16), 1813, doi:10.1029/2001GL014440.
- Palmén, E., and C. W. Newton (1969), *Atmospheric Circulation Systems*, pp. 112–114, Academic Press, San Diego, Calif.
- Pan, L. L., and L. A. Munchak (2011), Relationship of cloud top to the tropopause and jet structure from CALIPSO data, *J. Geophys. Res.*, *116*, D12201, doi:10.1029/2010JD015462.
- Pan, L. L., W. J. Randel, B. L. Gary, M. J. Mahoney, and E. J. Hints (2004), Definitions and sharpness of the extratropical tropopause: A trace gas perspective, *J. Geophys. Res.*, *109*, D23103, doi:10.1029/2004JD004982.
- Pan, L. L., et al. (2007), Chemical behavior of the tropopause observed during the Stratosphere-Troposphere Analyses of Regional Transport experiment, *J. Geophys. Res.*, *112*, D18110, doi:10.1029/2007JD008645.
- Pan, L. L., et al. (2010), The Stratosphere-Troposphere Analyses of Regional Transport 2008 experiment, *Bull. Am. Meteorol. Soc.*, *91*(3), 327–342, doi:10.1175/2009BAMS2865.1.
- Posselt, D. J., G. L. Stephens, and M. Miller (2008), CloudSat: Adding a new dimension to a classical view of extratropical cyclones, *Bull. Am. Meteorol. Soc.*, *89*(5), 599–609, doi:10.1175/BAMS-89-5-599.
- Randel, W. J., and E. J. Jensen (2013), Physical processes in the tropical tropopause layer and their roles in a changing climate, *Nat. Geosci.*, *6*(3), 169–176, doi:10.1038/ngeo1733.
- Ray, E. A., K. H. Rosenlof, E. Richard, D. Parrish, and R. Jakoubek (2004), Distributions of ozone in the region of the subtropical jet: An analysis of in situ aircraft measurements, *J. Geophys. Res.*, *109*, D08106, doi:10.1029/2003JD004143.
- Ridley, B. A., F. E. Grahek, and J. G. Walega (1992), A small high-sensitivity, medium-response ozone detector suitable for measurements from light aircraft, *J. Atmos. Oceanic Technol.*, *9*(2), 142–148, doi:10.1175/1520-0426(1992)009<0142:ASHSMR>2.0.CO;2.
- Riihimäki, L. D., and S. A. McFarlane (2010), Frequency and morphology of tropical tropopause layer cirrus from CALIPSO observations: Are isolated cirrus different from those connected to deep convection?, *J. Geophys. Res.*, *115*, D18201, doi:10.1029/2009JD013133.
- Shapiro, M. A. (1976), The role of turbulent heat flux in the generation of potential vorticity in the vicinity of upper-level jet stream systems, *Mon. Weather Rev.*, *104*(7), 892–906, doi:10.1175/1520-0493(1976)104<0892:TROTHF>2.0.CO;2.
- Shapiro, M. A., and S. Gronas (Eds.) (1999), *The Life Cycles of Extratropical Cyclones*, pp. 139–185, Am. Meteorol. Soc., Boston, Mass.
- Solomon, S., K. H. Rosenlof, R. W. Portmann, J. S. Daniel, S. M. Davis, T. J. Sanford, and G.-K. Plattner (2010), Contributions of stratospheric water vapor to decadal changes in the rate of global warming, *Science*, *327*(5970), 1219–23, doi:10.1126/science.1182488.
- Spichtinger, P., and K. M. Gierens (2009a), Modelling of cirrus clouds—Part 1b: Structuring cirrus clouds by dynamics, *Atmos. Chem. Phys.*, *9*, 707–719.
- Spichtinger, P., and K. M. Gierens (2009b), Modelling of cirrus clouds—Part 2: Competition of different nucleation mechanisms, *Atmos. Chem. Phys.*, *9*, 2319–2334.
- Spichtinger, P., and M. Krämer (2013), Tropical tropopause ice clouds: A dynamic approach to the mystery of low crystal numbers, *Atmos. Chem. Phys.*, *13*(19), 9801–9818, doi:10.5194/acp-13-9801-2013.
- Spichtinger, P., K. Gierens, and W. Read (2003), The global distribution of ice-supersaturated regions as seen by the Microwave Limb Sounder, *Q. J. R. Meteorol. Soc.*, *129*(595), 3391–3410, doi:10.1256/qj.02.141.
- Spichtinger, P., K. Gierens, and H. Wernli (2005a), A case study on the formation and evolution of ice supersaturation in the vicinity of a warm conveyor belt's outflow region, *Atmos. Chem. Phys.*, *5*, 973–987.
- Spichtinger, P., K. Gierens, and A. Dörnbrack (2005b), Formation of ice supersaturation by mesoscale gravity waves, *Atmos. Chem. Phys.*, *5*(5), 1243–1255, doi:10.5194/acp-5-1243-2005.
- Tilmes, S., et al. (2010), An aircraft-based upper troposphere lower stratosphere O<sub>3</sub>, CO, and H<sub>2</sub>O climatology for the Northern Hemisphere, *J. Geophys. Res.*, *115*, D14303, doi:10.1029/2009JD012731.
- World Meteorological Organization (1975), *International Cloud Atlas: Volume I—Manual on the observation of clouds and other meteors*, Geneva, p. 16.
- World Meteorological Organization (1987), *International Cloud Atlas*, vol. II Geneva, pp. 89–192.
- Wylie, D. P. (2002), *Cirrus and Weather*, pp. 136–146, Oxford Univ. Press, New York.
- Yang, Q., Q. Fu, and Y. Hu (2010), Radiative impacts of clouds in the tropical tropopause layer, *J. Geophys. Res.*, *115*, D00H12, doi:10.1029/2009JD012393.
- Zahn, A., E. Christner, P. F. J. van Velthoven, A. Rauthe-Schöch, and C. A. M. Brenninkmeijer (2014), Processes controlling water vapor in the upper troposphere/lowermost stratosphere: An analysis of 8 years of monthly measurements by the IAGOS-CARIBIC observatory, *J. Geophys. Res. Atmos.*, *119*, 11,505–11,525, doi:10.1002/2014JD021687.
- Zondlo, M. A., M. E. Paige, S. M. Massick, and J. A. Silver (2010), Vertical cavity laser hygrometer for the National Science Foundation Gulfstream-V aircraft, *J. Geophys. Res.*, *115*, D20309, doi:10.1029/2010JD014445.